



# **Efficient Energy Harvesting Interface for Implantable Biosensors**

JANKO KATIC

Licentiate Thesis  
in Information and Communication Technology  
KTH Royal Institute of Technology  
Stockholm, Sweden 2015

TRITA-ICT/MAP AVH Report 2015:02  
ISSN 1653-7610  
ISRN KTH/ICT-MAP/AVH-2015:02-SE  
ISBN 978-91-7595-497-4

KTH School of Information and  
Communication Technology  
SE-164 40 Kista  
SWEDEN

Akademisk avhandling som med tillstånd av Kungl Tekniska högskolan framlägges till offentlig granskning för avläggande av teknologie licentiatexamen i Mikro- och nanoelektronik onsdagen den 6 maj 2015 klockan 13.00 i Sal C, Electrum, Kungl Tekniska högskolan, Isafjordsgatan 22, Kista.

© Janko Katic, May 2015

Tryck: Universitetsservice US AB

## Abstract

Energy harvesting is identified as a promising alternative solution for powering implantable biosensors. It can completely replace the batteries, which are introducing many limitations, and it enables the development of self-powered implantable biosensors. An interface circuit is necessary to correct for differences in the voltage and power levels provided by an energy harvesting device from one side, and required by biosensor circuits from another. This thesis investigates the available energy harvesting sources within the human body, selects the most suitable one and proposes the power management unit (PMU), which serves as an interface between a harvester and biosensor circuits. The PMU targets the efficient power transfer from the selected source to the implantable biosensor circuits.

Based on the investigation of potential energy harvesting sources, a thermoelectric energy harvester is selected. It can provide relatively high power density of  $100 \mu\text{W}/\text{cm}^2$  at very low temperature difference available in the human body. Additionally, a thermoelectric energy harvester is miniature, biocompatible, and it has an unlimited lifetime.

A power management system architecture for thermoelectric energy harvesters is proposed. The input converter, which is the critical block of the PMU, is implemented as a boost converter with an external inductor. A detailed analysis of all potential losses within the boost converter is conducted to estimate their influence on the conversion efficiency. The analysis showed that the inevitable conduction and switching losses can be reduced by the proper sizing of the converter's switches and that the synchronization losses can be almost completely eliminated by an efficient control circuit. Additionally, usually neglected dead time losses are proved to have a significant impact in implantable applications, in which they can reduce the efficiency with more than 2%.

An ultra low power control circuit for the boost converter is proposed. The control is utilizing zero-current switching (ZCS) and zero-voltage switching (ZVS) techniques to eliminate the synchronization losses and enhance the efficiency of the boost converter. The control circuit consumes an average power of only 620 nW. The boost converter driven by the proposed control achieves the peak efficiency higher than 80% and can operate with harvested power below  $5 \mu\text{W}$ . For high voltage conversion ratios, the proposed boost converter/control combination demonstrates significant efficiency improvement compared to state-of-the-art solutions.

**Keywords:** Implantable biosensors, thermoelectric energy harvesting, energy harvesting interface, power management, DC-DC converters, dead time losses.

## Acknowledgements

Firstly, I would like to thank my supervisor, Prof. Ana Rusu, for giving me an opportunity to pursue a PhD at KTH in the exciting field of biomedical electronics. I am extremely grateful for her guidance, support and patience. I am also thankful to her for teaching me many lessons which stretch beyond electronics and scientific research. Her energy, work ethics and expertise make her an excellent role model to follow in my future career.

I would like to extend my sincerest gratitude to my co-supervisor, Dr. Saul Rodriguez, for sharing with me his knowledge, experience and skills in circuit design. I am also thankful to him for numerous discussions, valuable advices and constructive criticism. A special gratitude to his cheerful spirit, which is especially useful during long Swedish winters.

I acknowledge Swedish Research Council (VR) for funding my research.

I am also thankful to all members of the Integrated Circuits and Systems group, past and present. Sha Tao, my officemate, for being friendly and helpful from the first day I set foot in Sweden. Tingsu Chen for being a great colleague and neighbor. Nikola Ivanišević, Muhammad Waqar Hussain and Panagiotis Chaorani for many interesting conversations during lunch and coffee breaks. Time spent in Electrum would not be the same without you. Giuseppe Forestiere, my first supervised Master student, for making me proud. Jiazou Chi for simply being awesome.

I would like to extend my gratitude to all my friends/colleagues in Electrum: Jia Mao, Babak Taghavi, Anders Eklund, Saleh Kargarrazi, Ye Tian, Raheleh Hedayati, Dr. Maziar Naiini, Ganesh Jayakumar and Anderson Smith. I am also thankful to all my other friends around the world.

I would like to thank Prof. Jonny Johansson for accepting the role as an opponent at my defense. I would also like to express my gratitude to Dr. Per-Erik Hellström for reviewing my licentiate thesis.

My appreciation also goes to various people for participating my design review: Dr. Ernst Habekotté from Catena Microelectronics, Dr. Håkan Bengtsson and Örjan Renström from Ericsson AB, Dr. Martin Gustafsson from Maxim Integrated, Allan Olson, Jörgen Edvinsson and Lars Karlsson from Exploric AB. I am especially grateful to Dr. Ernst Habekotté for sharing many tips and tricks in circuit design with me, as well as for convincing me of the importance and beauty of hand calculations.

Gracious appreciation also goes to Prof. Mikael Östling and Prof. Carl-Mikael Zetterling for excellent management, which makes EKT beautiful and exciting working environment. I would like to thank Gunilla Gabrielsson for her kind help.

I would like to thank my lovely girlfriend Anja for her understanding, support and unconditional love. Finally, I want to thank my wonderful family, above all, my parents and my brother for encouraging and supporting me through all my life.

*Janko Katic,*  
Stockholm, March 2015



## Abbreviations and Acronyms

|      |   |
|------|---|
| AC   | Alternating current                     |
| AM   | Amplitude modulation                    |
| CMOS | Complementary metal-oxide semiconductor |
| DBS  | Deep brain stimulation                  |
| DC   | Direct current                          |
| DCM  | Discontinuous conduction mode           |
| ECG  | Electrocardiogram                       |
| EMG  | Electromyography                        |
| ESD  | Electrical static discharge             |
| ESR  | Equivalent series resistance            |
| FM   | Frequency modulation                    |
| IC   | Integrated circuit                      |
| IVSB | Inductor volt-second balance            |
| MEMS | Micro-electro-mechanical systems        |
| MIM  | Metal-insulator-metal                   |
| MPE  | Maximum power extraction                |
| MPPT | Maximum power point tracking            |
| NEMS | Nano-electro-mechanical systems         |
| NFET | N-field-effect transistor               |
| PCB  | Printed circuit board                   |
| PFET | P-field-effect transistor               |
| PFM  | Pulse frequency modulation              |
| PMU  | Power management unit                   |
| PWM  | Pulse width modulation                  |
| RF   | Radio frequency                         |
| RMS  | Root mean square                        |
| SMPS | Switched-mode power supply              |

|      |                             |
|------|-----------------------------|
| TEC  | Thermoelectric cooler       |
| TEG  | Thermoelectric generator    |
| TGFF | Transmission-gate flip flop |
| WBAN | Wireless body area network  |
| WSN  | Wireless sensor network     |
| ZCS  | Zero current switching      |
| ZVS  | Zero voltage switching      |

# Contents

|  |            |
|--|------------|
| <b>Contents</b>  | <b>vii</b> |
| <b>List of Figures</b>                                     | <b>ix</b>  |
| <b>List of Tables</b>                                      | <b>xi</b>  |
| <b>1 Introduction</b>                                      | <b>1</b>   |
| 1.1 Background on Implantable Biosensors . . . . .         | 1          |
| 1.2 Motivation . . . . .                                   | 4          |
| 1.3 Objectives . . . . .                                   | 6          |
| 1.4 Thesis Outline . . . . .                               | 7          |
| 1.5 Contributions and Publications . . . . .               | 8          |
| <b>2 Enabling Battery Free Biosensors</b>                  | <b>11</b>  |
| 2.1 Power Requirements of a Biosensor . . . . .            | 11         |
| 2.2 Power Autonomy . . . . .                               | 13         |
| 2.3 System Architecture . . . . .                          | 15         |
| 2.4 Summary . . . . .                                      | 15         |
| <b>3 Energy Harvesting</b>                                 | <b>17</b>  |
| 3.1 Background on Energy Harvesting . . . . .              | 17         |
| 3.2 Available Sources for Implantable Harvesting . . . . . | 19         |
| 3.2.1 Vibration Energy Harvesting . . . . .                | 19         |
| 3.2.2 Thermal Energy Harvesting . . . . .                  | 23         |
| 3.2.3 Biochemical Energy Harvesting . . . . .              | 28         |
| 3.2.4 Ambient RF Energy Harvesting . . . . .               | 30         |
| 3.3 Comparison and Discussion . . . . .                    | 31         |
| <b>4 Power Management Unit</b>                             | <b>35</b>  |
| 4.1 Input Step-up Converter Design . . . . .               | 36         |
| 4.2 Loss Mechanisms . . . . .                              | 41         |
| 4.2.1 Conduction Losses . . . . .                          | 42         |
| 4.2.2 Switching Losses . . . . .                           | 43         |

|          |  |           |
|----------|--|-----------|
| 4.2.3    | Synchronization Losses . . . . .         | 44        |
| 4.3      | Impact of Losses on Efficiency . . . . . | 50        |
| 4.4      | Maximum Power Extraction . . . . .       | 52        |
| 4.5      | Start-up Circuitry . . . . .             | 54        |
| 4.6      | Summary . . . . .                        | 54        |
| <b>5</b> | <b>Low Power Control</b>                 | <b>55</b> |
| 5.1      | Proposed Control Architecture . . . . .  | 55        |
| 5.2      | Driving the nFET Switch . . . . .        | 58        |
| 5.3      | Zero-Current Switching . . . . .         | 60        |
| 5.4      | Zero-Voltage Switching . . . . .         | 62        |
| 5.5      | Simulation Results . . . . .             | 64        |
| 5.6      | Summary . . . . .                        | 65        |
| <b>6</b> | <b>Conclusion and Future Work</b>        | <b>67</b> |
|          | <b>Bibliography</b>                      | <b>69</b> |

# List of Figures

|     |   |    |
|-----|---|----|
| 1.1 | Wireless body area network connected to a portable device. . . . .  | 1  |
| 1.2 | Typical biosensor system block diagram. . . . .   | 3  |
| 1.3 | Implantable biosensor examples: (a) First fully implantable pacemaker [11], (b) Modern miniature biosensor [13], (c) Cochlear implant [16]. . . | 3  |
| 1.4 | Alternative solution for powering implantable biosensors. . . . .   | 5  |
| 1.5 | Comparison between battery and energy harvesting powered biosensors [27]. . . . .   | 6  |
| 2.1 | Power consumption of a biosensor during one complete cycle [27]. . . . .  | 12 |
| 3.1 | General model of vibration harvester [52]. . . . .  | 21 |
| 3.2 | Comb-shaped capacitor for electrostatic energy harvesting [56]. . . . .   | 22 |
| 3.3 | Piezoelectric energy harvester structure [58]. . . . .  | 23 |
| 3.4 | Thermocouple. . . . .   | 24 |
| 3.5 | Equivalent models of a thermal energy harvester: (a) Electrical equivalent circuit, (b) Thermal model [65]. . . . .                             | 25 |
| 3.6 | Modeled tissue temperature profile under the skin surface [67]. . . . .   | 27 |
| 3.7 | Comparison of temperature differences across a single and multiple TEGs [68]. . . . .   | 27 |
| 3.8 | Glucose biofuel cell [74]. . . . .  | 28 |
| 3.9 | Fuel cells fabricated on silicon wafer [80]. . . . .  | 30 |
| 4.1 | Block diagram of the PMU. . . . .   | 36 |
| 4.2 | Simplified schematic of the boost converter. . . . .  | 38 |
| 4.3 | Switching diagram of the boost converter. . . . .   | 39 |
| 4.4 | Boost converter schematic. . . . .  | 41 |
| 4.5 | Schematic of a boost converter with parasitics. . . . .   | 42 |
| 4.6 | Detailed switching diagram during the pFET ON time [35]. . . . .  | 45 |
| 4.7 | Detailed switching diagram during the dead time. . . . .  | 47 |
| 4.8 | Equivalent circuit of the boost converter during the dead time [102]. . .   | 48 |
| 4.9 | Simple input matching. . . . .  | 53 |
| 5.1 | Block diagram of the traditional control circuit. . . . .   | 56 |

|      |   |    |
|------|---|----|
| 5.2  | Block diagram of the proposed control circuit. . . . .  | 57 |
| 5.3  | Level shifter schematic. . . . .  | 58 |
| 5.4  | Switch driver schematic. . . . .  | 58 |
| 5.5  | nFET switch signal generator [105]. . . . .   | 59 |
| 5.6  | Waveforms of a pFET switch turning off (a) slightly early, (b) early and<br>(c) late [105]. . . . . | 61 |
| 5.7  | pFET switch signal generator [105]. . . . .   | 62 |
| 5.8  | Adaptive dead time circuit [102]. . . . .   | 63 |
| 5.9  | Efficiency comparison between [35] and this work. Image from [105]. . .                             | 64 |
| 5.10 | Waveform of the voltage $V_X$ [105]. . . . .  | 65 |
| 5.11 | Efficiency improvement due to the adaptive dead time [102]. . . . .                                 | 66 |

# List of Tables

|     |  |    |
|-----|--|----|
| 2.1 | Comparison of batteries and supercapacitor [27, 45]. . . . .                       | 14 |
| 3.1 | Comparison of potential energy harvesting sources for implantable devices. . . . . | 32 |
| 5.1 | Adjusting the counter value according to the sensed signal. . . . .                | 61 |
| 5.2 | $\tau_P$ , decoder outputs and dead time corresponding to counter values. . . . .  | 63 |
| 5.3 | Parameters of the proposed boost converter. . . . .                                | 65 |
| 5.4 | Comparison of the proposed boost converter with state-of-the-art work. . . . .     | 66 |





# Chapter 1

## Introduction

### 1.1 Background on Implantable Biosensors

Wireless sensor networks (WSNs) have received much attention in the past decade. Their popularity was driven by the wide range of potential applications to industry, science, military, security and infrastructure [1, 2]. The application areas include lifesaving systems, such as the fire detection [3] or bridge monitoring systems [4]. Recent technology development and device miniaturization have facilitated building

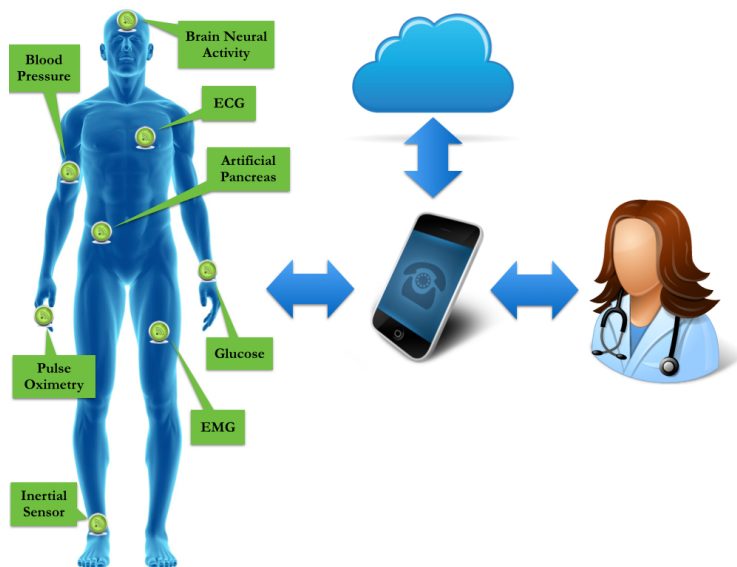


Figure 1.1: Wireless body area network connected to a portable device.

smaller and smarter sensors. In particular, CMOS electronics and radio communication circuits have further decreased their size and improved their performance, speed and power consumption [5]. At the same time, micro-electro-mechanical systems (MEMS) technology has advanced towards nano-electro-mechanical systems (NEMS) enabling the development of new types of smart sensors [6]. As a result, new applications of WSN are emerging on a daily basis, which further increase their popularity. Currently, one of the most attractive, potentially lifesaving application is health monitoring.

Wireless sensor networks responsible for health monitoring are called wireless body area networks (WBANs). A sensor node, which converts a biological signal into an electrical signal, is rather addressed as a biosensor. It is also important to clarify that a modern biosensor is not only converting the signal but it is a small system itself, capable of processing and sending the sensed signal. Such interpretation of a biosensor is adopted in this work. WBANs are made of distributed wearable or implantable biosensors. The general purpose of WBAN is to continuously monitor the patients' health or overall well-being and to warn the patient if some reading is outside the normal range. The ultimate goal is to connect these biosensor networks with portable devices in order to access the information easier or automatically send the readouts to a health care institution, as it is illustrated in Fig. 1.1. Such systems may have tremendous potential for diagnostic and prevention purposes depending on the incorporated types of biosensors and their functionality [7]. For this reason, further improving already existing biosensors, and developing new biosensors is essential for the future evolution of health monitoring systems. However, many challenges have to be tackled on this journey, considering the biosensor requirements related to powering, reliability, accuracy, etc.

A sensing device is closely combined with its corresponding readout circuitry, analog-to-digital converter, digital signal processing, communication and powering devices to form a single biosensor, as it is shown in Fig. 1.2. Today, there are medical applications which favor implantable biosensors, due to advantages provided by the direct access to an analyte [8]. In fact, some applications, such as deep brain stimulation (DBS) [9], demand implantable biosensors since it is the only way to access the bioinformation. Compared to non-invasive biosensors, implantable biosensors have even more strict constraints and limitations in terms of size, power, biocompatibility and lifetime, which make their development very challenging.

The idea of continuous monitoring and stimulating patient's health conditions using an implantable device originates from many years ago [10]. The first fully implantable pacemaker, shown in Fig. 1.3(a) [11], was implanted into the human body back in 1958 [10]. However, the concept of WBAN was firstly introduced in 2001 [12], decades later. This is because all different fields contributing to the evolution of such systems have reached the required level of development only recently. The technology innovations and device miniaturization allow to squeeze the whole biosensor system into an extremely small volume, as it is shown in Fig. 1.3(b) [13]. Consequently, many new applications of implantable biosensors appeared. The earliest implantable medical devices were for monitoring and stimulating the human

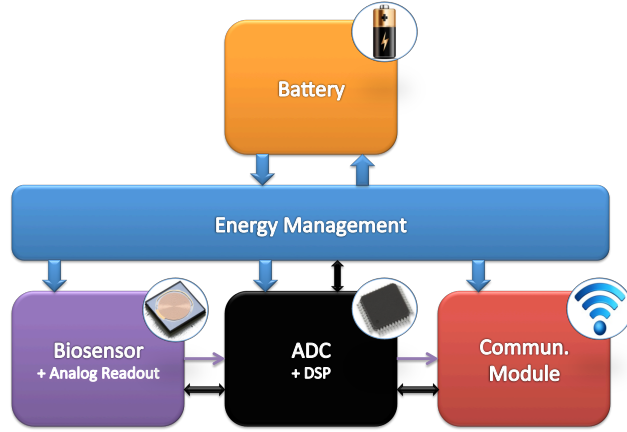


Figure 1.2: Typical biosensor system block diagram.

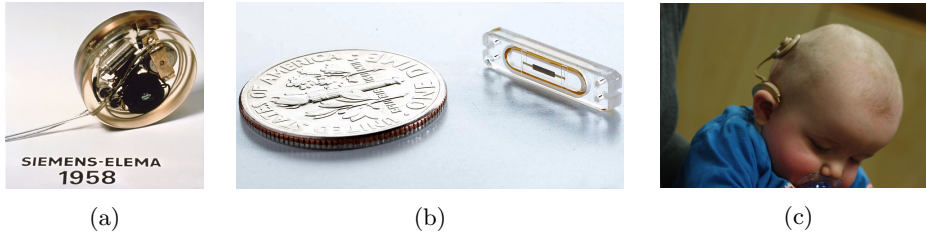


Figure 1.3: Implantable biosensor examples: (a) First fully implantable pacemaker [11], (b) Modern miniature biosensor [13], (c) Cochlear implant [16].

heart, known as pacemakers and defibrillators [14,15]. By fighting against ventricular tachycardia and cardiac arrhythmia, those devices saved many lives in the past, and they are still saving lives today. Other well-known implantable devices are the cochlear implant for hearing aids [17], as illustrated in Fig. 1.3(c) [16], and the retinal implant (partial vision restore) [18]. Relatively new applications include blood pressure monitoring [19] for hypertension, glucose monitoring [20] for diabetes and monitoring the brain neural activity [21] for a wide variety of neural disorders. For instance, for a patient with Parkinson disease, the implantable device is capable of predicting and stopping any tremors to occur by monitoring the specific brain activity and providing the proper stimulation [22]. Monitoring of the brain neural activity could also help patients with epilepsy, paralysis, chronic pain, dystonia and even depression [23].

The reliable functionality and the proper communication with the outside world dictate strict performance requirements for the whole implantable biosensor and all its individual blocks [24]. The biosensor has to meet several vital prerequisites just in order to be considered appropriate for implantation [8]. The complete system needs to be very small (less than  $\text{cm}^3$ ), so that the patient feels comfortable with the device and implantation procedure. It has to be biocompatible to avoid an unexpected immune response, implant rejection or injurious effects. Furthermore, in order to meet the power requirements, the power consumption of the complete system needs to be very low. Finally, the lifetime of the device should be as long as possible; in the ideal case, it should exceed the lifetime of the host. So, once the device is implanted, no additional maintenance should take place for years. Today, the lifetime of implantable biosensors is mainly limited by batteries [25]. Constantly replacing the batteries is not an acceptable solution for implantable devices, because it requires a new surgical procedure whenever a battery is discharged. For this reason, alternative solutions for powering the biosensors are desired.

## 1.2 Motivation

The power consumption of an implantable biosensor is determined by many factors, such as its complexity, the nature of a sensed signal, the number of transmissions per second, and so on. Biosensors that consume less than  $20 \mu\text{W}$ , have already been reported [26]. However, the representative power consumption for biosensors with medium complexity and relatively high data-rate is  $100 \mu\text{W}$  [27]. Such biosensor would drain a  $1 \text{ cm}^3$  lithium battery in less than a year. This fact clearly shows that the long term powering of implantable biosensors is an extremely challenging task.

The majority of currently available implantable biosensors are powered by batteries, which have limited energy capacity and lifetime. Depending on the average power consumption of a biosensor, this limited time can range from a few days up to several years, so eventually battery replacement is unavoidable. Batteries have a dominant impact not only on the lifetime of an implantable biosensor, but also on its size. As it was already mentioned, the miniature size is one of the main requirements of implantable devices. On top of that, there are also many health concerns related to a battery implantation inside the human body. If mistreated, the potentially hazardous and toxic batteries can be very harmful to the patient. Finally, they are almost non-recyclable, which raises environmental issues, even if they are carefully disposed. Therefore, batteries can be considered as the bottleneck of today's implantable biosensor development. They represent the main obstacle toward fully autonomous, millimeter size and high-performance implantable biosensors. Finding alternative solutions in order to avoid constant battery replacement is the primary goal of many recent investigations [27–34].

One very attractive solution for building autonomous systems is energy harvesting. Energy harvesting is a process that exploits small amounts of energy from

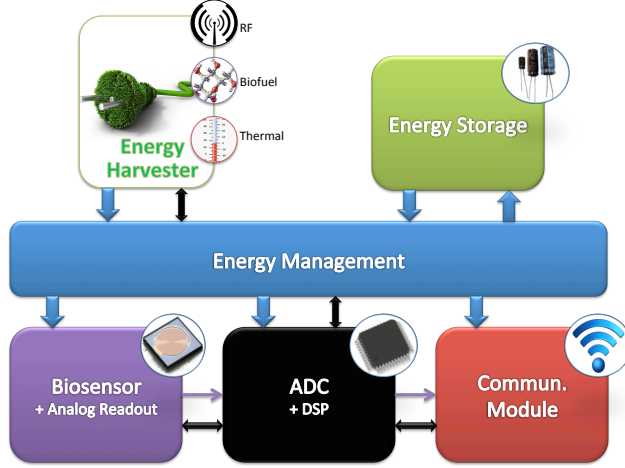


Figure 1.4: Alternative solution for powering implantable biosensors.

the environment, which would otherwise be lost, such as heat, light, vibration, etc. One simple example of energy harvesting devices is a solar panel, which transforms solar energy to electrical energy. An energy harvester can be used to recharge the battery, and by doing so, it decreases the size and prolongs the lifetime of the battery. However, even if the battery is recharged, it still has a limited lifetime due to the relatively low number of cycles (cycle life). Instead of using a rechargeable battery, a large capacitor or a supercapacitor, with an almost unlimited number of cycles, can be used as an energy storage device. In this case, the system becomes battery-free, as it is shown in Fig. 1.4. Therefore, energy harvesting can even completely replace the battery [33]. In addition, it has the potential to make the system fully autonomous. The power consumption versus operation time (lifetime) of the biosensor for both powering schemes is illustrated in Fig. 1.5 [27]. It is obvious, from the figure, that the system which combines energy harvesting with the energy storage device can easily outperform the traditional battery powered system in low power applications. In addition, if the average harvested power is higher than the average consumed power, such system can be fully autonomous and run indefinitely without any maintenance. However, for proper operation it requires a dedicated interface circuit, called power management unit (PMU). This is mainly because the output voltage of an energy harvester is usually very low and has to be converted to a much higher voltage required by the biosensors circuitry. The PMU is the main focus of this work and it will be covered in the forthcoming chapters.

There are many different energy harvesters, exploiting energy from various ambient sources, such as light, heat, motion, chemical reactions, etc. However, for micro-

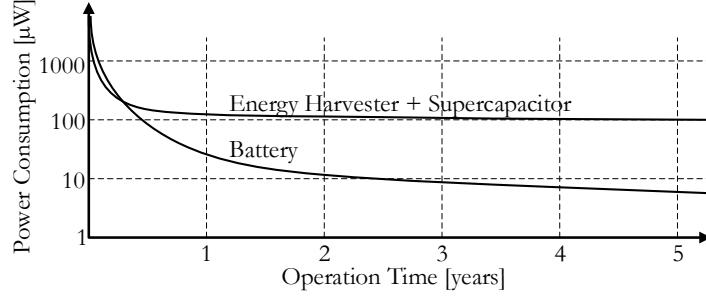


Figure 1.5: Comparison between battery and energy harvesting powered biosensors [27].

scale implantable devices only a few harvesting techniques can be used [28, 34]. A potential harvester should operate and extract energy from inside the human body, which is an unconventional and complex environment. So, the most suitable energy harvesting technique for powering implantable biosensors needs to be identified.

Since the power and the output voltage of a harvester are extremely low, the dedicated PMU encounters severe requirements and design challenges [27, 28, 32]. It should be able to efficiently convert input voltages in the order of tens of mV to voltages required by the biosensor. In order to maintain the relatively high efficiency, the PMU circuitry itself should consume only a small fraction of the overall available power, which can be as low as few  $\mu\text{W}$ . Efficient PMU solutions for various energy harvesting sources have been proposed in the literature [35–41]. However, only a few solutions are targeting ultra low power harvesting for implantable applications. It is still a relatively young research area with many challenges and a lot of space for new solutions or improvements of already existing ones. The focus of this work is to develop and design such a PMU for a selected energy harvesting technique which can enable self-powered implantable biosensors.

### 1.3 Objectives

The aim of this thesis is to propose and develop an efficient energy harvesting interface for implantable biosensors. In order to successfully reach this goal, four intermediate objectives have been addressed.

The first objective is to select an appropriate implantable energy harvester, which has potential to self-power the implantable biosensor. In order to do so, the available energy sources within the human body are investigated in detail. The selection is based on different criteria, such as the output power level per volume, output voltage, biocompatibility, size, etc.

The second objective is to propose a suitable power management unit architecture. The PMU acts as an interface between a harvester and biosensor circuits, so the proposed architecture should meet the loading requirements of the selected energy harvester as well as powering demands of the implantable biosensors. Additionally, it should be able to efficiently transfer the harvested energy to the biosensor circuitry. To achieve this objective, potential power management architectures and their critical building blocks (i. e. input step-up converters) are explored and examined considering the system constraints.

The third objective is to develop and implement techniques for minimizing losses within the PMU and the power consumption. This objective is important for maximizing the efficiency of energy transfer from the harvester to the biosensor circuitry. The goal is to successfully locate and suppress all potential losses. For this reason, the extensive analysis of different loss mechanisms within the converter and their impact on the overall efficiency is carried out.

The fourth objective is to design and verify an efficient energy harvesting power management unit for powering implantable biosensors. The PMU should utilize and validate all previously developed techniques for minimizing the related losses and the power consumption of the control circuitry, a critical part of the PMU. It should be highly efficient even at very low input voltage and power levels.

## 1.4 Thesis Outline

This thesis is organized in six chapters as follows:

- Chapter 1 introduces the implantable biosensors, their importance and potential application fields. It also presents the motivation, objectives, outline and contributions of this work.
- Chapter 2 discusses the system level architecture of implantable biosensors. It focuses on the powering requirements and introduces the energy storage device. Challenges towards fully autonomous battery-free systems are also addressed.
- Chapter 3 provides the background on energy harvesting. It also presents an overview of the existing state-of-the-art micropower energy harvesting sources. The potential sources for powering implantable biosensors are reviewed and compared against each other. Finally, the most suitable one is singled out.
- Chapter 4 presents the proposed power management unit. Requirements and constraints dictated by the energy harvesting source from one side and the biosensor circuitry from the other are both discussed and explained. The top level architecture and the individual building blocks are described. The design procedure of the boost converter, the critical block of the PMU, is defined. Additionally, the loss mechanisms inside the input converter are analyzed in detail. Finally, ideas for maximum power extraction, start-up circuits and efficient control of the input converter are introduced.
- Chapter 5 presents the design of the ultra low power control circuits for the proposed PMU. This chapter also describes the techniques to achieve the high

conversion efficiency, including Zero-Current Switching (ZCS) and Zero-Voltage Switching (ZVS). Finally, the design of the nanowatt power building blocks as well as the implementation of these techniques are presented.

- Chapter 6 draws the conclusions and identifies the future directions.

## 1.5 Contributions and Publications

Based on the extensive investigation of all potential micropower harvesting sources for implantable biosensors, the thermoelectric energy harvesting is selected. Thermoelectric energy harvesting provides relatively high output power densities, small size, biocompatibility and good reliability due to the ubiquitous temperature gradient inside the human body. Assuming 1 K temperature difference, the thermoelectric harvester can theoretically provide up to  $100 \mu\text{W}/\text{cm}^2$ , which should be enough for powering implantable biosensors in most applications. In addition, its equivalent electrical circuit is rather simple so that the maximum power extraction (MPE) is somewhat straightforward. Further on, based on the selected energy harvesting source, the corresponding power management system architecture is proposed. A boost converter with an external inductor is employed as the input step-up converter. This type of converter can be efficient at low power levels and maintain the high efficiency even at high voltage conversion ratios. At the same time, its input resistance can be controlled and easily matched to the internal resistance of the thermoelectric device to enable the maximum power extraction. Finally, the boost converter can provide the adequate supply voltage for the biosensor circuitry.

To obtain high efficiency, an extensive analysis of the losses within the boost converter is performed. As a result, simple expressions for estimating all relevant losses and their impact on the system efficiency are derived. The analysis showed that the usually neglected dead time losses are significant for implantable applications. The overall efficiency reduction due to these losses can easily exceed 2%. Based on these findings, two techniques are proposed to suppress the inevitable losses, eliminate the dead time losses and obtain zero-current and zero-voltage switching, simultaneously. Furthermore, an ultra low power control for the boost converter is designed. The aforementioned techniques are implemented and employed in the control circuits. The control is mostly digital, and its building blocks are carefully designed and customized for ultra low power operation. The whole control consumes an average power of 620 nW. Consequently, it enables the PMU to achieve high efficiency under the strict power requirements.

Finally, the design procedure of the boost converter is defined. All sizes and values of different parameters and components of the input converter are carefully calculated and selected so that the losses are minimized. Consequently, a very efficient boost converter is designed. The peak efficiency of the converter is higher than 80% and it is maintained even at very high conversion ratios and low input power. The designed converter can operate with very low input voltages of a few tens of mV and, at the same time, can achieve the maximum power extraction from



the harvesting source.

These research contributions have resulted in the following publications:

- J. Katic, S. Rodriguez, and A. Rusu, “An Efficient Boost Converter Control for Thermoelectric Energy Harvesting,” in *Proceedings of IEEE International Conference on Electronics, Circuits and Systems (ICECS)*, Abu Dhabi, UAE, December 2013, pp. 385-388.

Author’s contribution: 100% theoretical analysis, 100% IC design, 90% of writing the manuscript.

- J. Katic, S. Rodriguez, and A. Rusu, “Analysis of Dead Time Losses in Energy Harvesting Boost Converters for Implantable Biosensors,” in *Proceedings of IEEE Norchip Conference*, Tampere, Finland, October 2014, pp. 1-4.

Author’s contribution: 100% theoretical analysis, 100% IC design, 90% of writing the manuscript.



## Chapter 2

# Enabling Battery Free Biosensors

In order to evaluate the potential for developing battery free biosensors, it is essential to investigate the power requirements of biosensor circuits, as well as the obtainable power and voltage levels of energy harvesting devices. In fact, it is expected that there will be some discrepancies between the available and required power and voltage levels. This is because the biosensor circuits generally require stable voltage supplies in the range of 1 - 2 V. In addition, the power consumption of the biosensors circuits can be quite high, reaching tens of mW during some periods of their operation. On the other hand, the output power and voltage levels provided by the energy harvesters are usually low and unpredictable; they might be as low as a few  $\mu\text{W}$  and tens of mV respectively. The power management unit (PMU) acts as an interface between the energy harvester and the biosensor circuits and it is used to adjust for these differences, as it is shown in Fig. 1.4. The PMU is crucial for enabling battery free biosensors. However, before engaging in more details about the PMU, it is necessary to define and clarify its primary tasks and requirements dictated by the biosensor circuitry from one side and the energy harvesting device from another.

In this chapter, the power consumption patterns and the required voltage supplies for implantable biosensors will be evaluated for various applications. Additionally, the system requirements for autonomous operation will be discussed. The potential output power and voltage levels of available energy harvesting sources and more details on the PMU will be covered in forthcoming chapters.

### 2.1 Power Requirements of a Biosensor

In general, the power consumption of implantable biosensors greatly depends on the application. The applications that require continuous monitoring, in which large amount of data is transferred, are usually power demanding. On the other hand, the occasional sensing and a small amount of transferred data correspond to low power consumption. For instance, continuous sensing, processing and transmitting

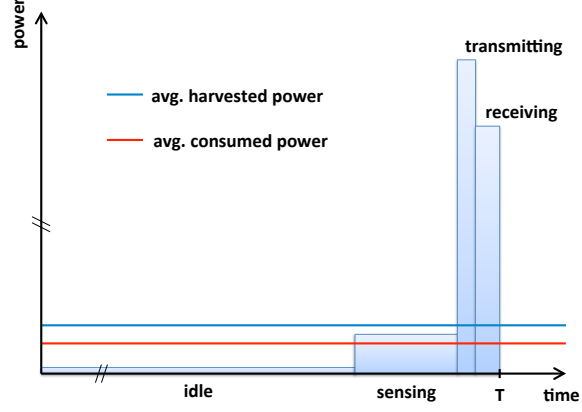


Figure 2.1: Power consumption of a biosensor during one complete cycle [27].

the neural brain activity is far more power hungry than sensing and sending the temperature once in every hour. This is because most of power is consumed while receiving and transmitting relevant data. However, the majority of biomedical applications require only a limited amount of exchanged information [42]. Many biosensors sense, transmit and receive information infrequently, meaning that they are inactive most of the time. A typical power demand pattern of an implantable biosensor is illustrated in Fig. 2.1 [27]. Significant variations in the power demand during the same working cycle are evident, ranging from less than  $1 \mu\text{W}$  during the idle phase, up to tens of  $\text{mW}$  during transmission.

As it can be seen in Fig. 2.1, the average power consumption is strongly affected by the duration of the idle (sleep) state. In fact, in some cases, the average power consumption can be adjusted by changing the duration of this state, or in other words by changing the operating duty cycle of the biosensor. For example, assume that it is necessary to decrease the average power consumption of a glucose monitoring implantable biosensor. If the power consumption in the sleep mode is neglected for simplicity, by measuring and sending data once in every 5 minutes instead of every 1 minute, the average power consumption of a sensor is reduced more than five times. Note that this is applicable only when the particular application allows decreasing the duty cycle. Suppose that  $D$  is the operation duty cycle of the biosensor, then its active state lasts for  $DT$ , where  $T$  is the complete cycle period. For simplicity, sensing, transmitting and receiving phases are all considered as an active state, with an overall average power of  $P_{\text{active}}$ . The average power of the idle state is  $P_{\text{sleep}}$ . Then the average power consumed by the biosensor is [43]:

$$P_c = DP_{\text{active}} + (1 - D)P_{\text{sleep}}. \quad (2.1)$$

Eq. (2.1) can be further simplified by assuming that the biosensor does not consume any power during the idle state. For  $P_{sleep} = 0$  the average power is:

$$P_c = DP_{active}. \quad (2.2)$$

It is evident from Eq. (2.2) that the average power consumption can be reduced by decreasing the duty cycle. However, it is important to note that this is not possible in the applications which have a strictly defined data transfer rate.

The biosensor requires a stable power supply voltage for proper operation. In fact, because it consists of different RF, analog and digital sub-blocks, it usually requires several various power supply voltages. Having multiple power supplies is beneficial primary in terms of power savings. The supply voltage and, consequently, the power consumption of individual blocks can be customized. For instance, digital circuits might be fast enough with just half of the voltage supply required by the RF circuitry. On top of that, digital circuits generate supply noise due to their switching characteristics and high feedthrough currents. This noise is undesirable for the RF circuitry that requires a relatively "clean" supply voltage. So, having separate power supplies prevents this problem and reduces the overall power consumption [44].

During the active state of the biosensor and especially during the data transmission, the required current levels can exceed 10 mA [42]. The aforementioned high power demand during the transmission is actually a reflection of these currents. The high currents can cause a significant voltage drop in the high impedance voltage source. Therefore, the power supplies for a biosensor have to be carefully designed to handle such variations in current levels.

## 2.2 Power Autonomy

Energy harvesting is a promising alternative to batteries and it can enable the autonomous powering of implantable biosensors. Using a harvester to directly power biosensor circuits requires that at any moment the instantaneous harvested power  $p_h(t)$  is higher than the instantaneous consumed power  $p_c(t)$ :

$$p_h(t) \geq p_c(t). \quad (2.3)$$

This condition is extremely difficult to achieve considering the previously presented power requirements of a biosensor. On top of that, harvested energy is quite unpredictable, and it might happen that it is the lowest at the moment when a biosensor is transmitting the data. For all these reasons, an energy storage device is necessary for most of the energy harvesting systems and particularly in implantable applications [42, 43]. The energy storage device should act as an energy buffer, which accumulates the energy during the low power demand periods, such as the idle state, and provides the excessive energy during the high power demand periods. There are three possible candidates for the energy storing devices: standard rechargeable batteries, emerging thin film batteries and supercapacitors. The problems related

Table 2.1: Comparison of batteries and supercapacitor [27, 45].

|                                      | Battery |           | Supercapacitor |
|--------------------------------------|---------|-----------|----------------|
|                                      | Li-ion  | Thin film |                |
| <b>Operating voltage (V)</b>         | 3.7     | 3.7       | 1.25           |
| <b>Energy density (Wh/l)</b>         | 435     | <50       | 6              |
| <b>Self-discharge rate (%/month)</b> | 1       | 1         | 100            |
| <b>Cycle life (cycles)</b>           | 2000    | 1000      | >10000         |
| <b>Temperature range (°C)</b>        | -20/50  | -20/70    | -40/65         |

to conventional batteries have already been identified. Thin film batteries, unlike conventional ones, can be integrated into the IC packages, fabricated on plastics, can have any shape or size and some of them are even flexible [27]. However, their energy density is much less than of the classical batteries and the number of cycles is still limited. Supercapacitors are electrochemical capacitors with very large capacitance values. Their performance is between the performance of batteries and conventional capacitors, as it can be seen in Table 2.1 [27, 45]. The energy density of supercapacitors is lower than the energy density of batteries, but their power density is much higher. Supercapacitors are capable of providing a high burst of power in a very short time frame [45, 46], which makes them well suited for implantable biosensors. A very large number of possible cycles makes their lifetime almost unlimited. Additionally, their safety is improved over batteries, and there is no danger of overcharging or exploding. Finally, the supercapacitor technology is very promising and it is evolving at a faster rate than the battery technology. All these features make supercapacitors a superior energy storage solution for implantable biosensor systems.

By introducing an energy storage device between the energy harvester and the biosensor circuits, the harvested power does not have to be always higher than the required power. During the high power demand, the power is provided by the storage device rather than the energy harvester. Consequently, it is sufficient that the average harvested power,  $P_h$ , is higher than the average power consumption of the biosensor,  $P_c$  [42, 43]:

$$P_h \geq P_c. \quad (2.4)$$

This condition is much easier to meet than the one defined by Eq. (2.3). By combining Eq. (2.4) with (2.1), the maximum allowable duty cycle,  $D_{max}$ , can be estimated as [43]:

$$P_h \geq DP_{active} + (1 - D)P_{sleep}, \quad (2.5)$$

$$D_{max} = \frac{P_h - P_{sleep}}{P_{active} - P_{sleep}}. \quad (2.6)$$

Further, the required energy capacity of the storage device can be estimated. The difference between the total energy consumed by the biosensor circuits,  $E_{con}$ , during one period of operation and the total energy generated by the energy harvester,  $E_{har}$ , should be provided by the energy storage device [42, 43]:

$$E_{con} = \int_T p_c(t) dt, \quad (2.7)$$

$$E_{har} = \int_T p_h(t) dt, \quad (2.8)$$

$$(2.9)$$

so the energy capacity of the storage element,  $E_{storage}$ , is given by:

$$E_{storage} \geq \max\{E_{con} - E_{har}\}, \quad (2.10)$$

$$E_{storage} \geq \max\left\{\int_T [p_c(t) - p_h(t)] dt\right\}. \quad (2.11)$$

Finally, if the condition in Eq. (2.4) is satisfied for an acceptable duty cycle and a reasonable size of the storage device, the autonomous powering of the biosensor is possible.

### 2.3 System Architecture

The block diagram of a biosensor system powered by an energy harvester is shown in Fig. 1.4. Compared to the traditional diagram in Fig. 1.2, the battery is replaced with the combination of an energy harvester and an energy storage device. The energy harvester extracts the energy from the environment. The PMU transfers the energy to a storage device, where it is accumulated during the whole idle period of the biosensor. Afterwards, during the active state of the biosensor, the accumulated energy is used to power the biosensor circuitry. The PMU is also responsible for the correct distribution of energy between the different blocks of the biosensor. Therefore, it is managing the complete energy transfer between the energy harvester, the storage device and the biosensor's building blocks. The energy transfers have to be efficient so that only a small fraction of energy is lost during this process. This is a rather simplified description of the energy transfer within the biosensor. In reality, achieving the efficient energy transfer while meeting the requirements of all different blocks at the same time, as well as accurate scheduling and monitoring the tasks, is quite challenging. This matter will be covered in more details in Chapter 4.

### 2.4 Summary

The amount of power that is needed for powering an implantable biosensor is application dependent. For this reason, it is impractical to define the power consumption

of a biosensor in general. At the same time, the power consumption of a particular biosensor is varying during its operating cycle. Two different states are distinguished, the idle (sleep) state during which the power consumption is low and the active state in which the power demand is high. An energy buffer, e. g. supercapacitor, is necessary to handle these high power demands. If the application allows altering the durations of the sleep and active states, the power consumption of the biosensor can be reduced by prolonging the sleep state. Finally, self-powered biosensors are achievable if the following conditions are satisfied. First, the average harvested power has to be higher than the average consumed power. Second, the energy storage device needs to have a sufficient energy capacity. Third, the power management unit has to transfer the energy efficiently from the energy harvester to the energy storage and biosensor's circuitry.



## Chapter 3

# Energy Harvesting

This chapter investigates the amount of power that can be provided by the energy harvester, and transferred to the PMU and further to the biosensor. This step is crucial in order to determine whether the autonomous powering of the biosensor is possible.

Energy harvesting has been identified as a potential alternative to batteries in many applications [47–49]. The output power of the energy harvester entirely depends on its environment and available energy in the vicinity. Accordingly, some applications are much more suitable for using the harvested energy than other. For this reason, it is essential to understand the environment of a potential application, to locate the possible sources for energy harvesting and their corresponding power levels.

### 3.1 Background on Energy Harvesting

Energy harvesting is a process which converts a small amount of energy from the environment into electrical energy. More informal description may be that energy harvesters are miniature green power plants. The amount of energy which defines the energy harvesting is not precisely specified. However, as a convention it is considered that for the energy harvesting which is intended for wireless sensor nodes or perhaps portable devices, "a small amount of energy" stands for a mW power range or less.

Energy harvesting for low power applications has gained much attention recently mainly as a consequence of the huge popularity of wireless sensor networks for a wide range of applications. It became practical due to technology advancements and extremely low power requirements of modern sensor nodes. In fact, the idea is not new. The early energy harvesting devices were developed decades ago. First, solar cells were introduced in 1950s. Then thermoelectric generators appeared in 1960s, when they were considered for co-integration with nuclear batteries to power early implantable pacemakers [50]. As a matter of fact, most of the fundamental effects,

on which the modern energy harvesting devices are based, such as the photovoltaic and Seebach effect, were discovered in the 19th century during the industrial revolution [47]. However, only recently it became possible that a complete sensor node, consisting of a readout circuitry, analog-to-digital converter, micro-controller unit and radio may operate in the microwatt range. This has opened the possibility of using alternative sources of energy, such as energy harvesting, to replace the batteries.

The energy harvester can be used to power any individual device or system which consumes a low amount of power, including sensor nodes. Therefore, the list of potential applications is almost limitless. Energy harvesting is especially suitable when the device is physically inaccessible or hard to reach. When compared to batteries, it is advantageous in terms of lifetime, size, safety and being environmentally-friendly. Nevertheless, there are many challenges that have to be overcome before energy harvesting can be used to power devices. First of all, the successful implementation of an energy harvesting device itself is very challenging and it is a multidisciplinary task. Secondly, the energy available for harvesting is usually variable and hard to predict, so the potential energy source has to be thoughtfully selected, and the amount of output energy carefully estimated. Thirdly, in most cases, the resulting output power and voltage are very low. They require conversion and adequate handling in order to be used by a sensor node or some other device. A dedicated PMU is necessary to perform this task. Finally, the energy harvesting device requires a matched load to provide the maximum possible output power. The PMU also ensures that the appropriate impedance is presented to the energy harvester. It is evident that the performance of energy harvesting heavily depends on the capabilities of the PMU.

There are various kinds of ambient energy sources from which the energy can be harvested. The well-known ones include natural energy sources, such as sunlight, wind or water flow. There are artificial sources too, for instance, waste heat, industrial vibrations or indoor light. Energy can be also harvested from some less known sources such as biochemical reactions or microwaves. Although it seems that there are potential energy harvesting sources in every situation, in reality, the amount of available energy is very dependent on the environment. In some cases, a considerable amount of energy might be on disposal for harvesting while in others there might be scarce energy available. Successful energy harvesting in environments with limited available energy is very demanding. Health monitoring based on implantable biosensors is one of the applications that require energy harvesting from such environments. In fact, the human body is one of the most challenging environments for energy harvesting. At the same time, potential benefits are also superior because every battery replacement requires a new surgical procedure for the patient. For this reason, it is important to carefully investigate the possible harvesting sources within the human body and to identify the most promising ones that can potentially be used to power a biosensor.

### 3.2 Available Sources for Implantable Harvesting

Implantable devices are completely surrounded by the human tissue. Their environment within the human body is dark, thermoregulated and lacks continuous motion. It is evident that it is not the best environment for energy harvesting. On top of that, implantable devices are subject to many strict regulations regarding the size, weight, reliability, biocompatibility, and so on. This is additionally limiting the usability of implantable energy harvesting. However, even in such unsuitable environment, potential energy harvesting sources exist, and they include the following:

- **Motion and vibration** – Different movement mechanisms are associated with the human body. There are occasional whole body movements, when a person is walking or running, and periodic movements, such as heart beating or lung movement while breathing. These movements and vibrations can potentially provide a certain amount of kinetic energy for harvesting.
- **Thermal** – Even though the human body is thermoregulated (tries to maintain the constant temperature), a small thermal gradient endures. The temperature of the body is slowly decreasing from the core of the body where it is the highest until it reaches the skin where it is the lowest. As a consequence, there are a few degrees of temperature difference available for energy harvesting.
- **Biochemical** – Some of the chemical compounds in the human body, such as glucose, contain energy in the form of chemical bonds. Under certain conditions, this energy can also be harvested.
- **Ambient RF** – Nowadays, especially in urban areas, there are many RF systems which are constantly communicating. The related RF microwaves are carrying certain amount of energy even after penetrating the human body. This energy is also available for energy harvesting.

It should be noted that the energy transfer using inductive coupling and the RF energy transfer with a dedicated energy source are excluded from the list of potential implantable energy harvesting sources. This is because they are considered here as an energy transfer method rather than energy harvesting.

#### 3.2.1 Vibration Energy Harvesting

Vibration energy harvesters capture the energy from the human motion and transform it into electrical energy. There are three main mechanisms for converting motion or vibration to electrical energy: electromagnetic, electrostatic and piezoelectric. A general model for converting the energy of a vibrating mass to electrical energy has been described in [51] for modeling electromagnetic converters. This model has been further expanded in [52] to cover the electrostatic and piezoelectric

converters more accurately. The final model does not require the specification of a particular conversion mechanism, since it is valid, to some extent, for all of them. The schematic of this universal model is shown in Fig. 3.1.

The system is described by [52]:

$$m\ddot{z} + (b_e + b_m)\dot{z} + kz = -m\ddot{y}, \quad (3.1)$$

where  $m$  is the mass,  $y$  is the input displacement,  $z$  is the spring deflection,  $k$  is the spring constant,  $b_e$  and  $b_m$  are the electrical and mechanical damping coefficients, respectively. The resulting electrical power is equal to the power collected by the electrically induced damping ( $b_e = 2m\xi_e\omega_n$ ). Considering that the power is the product of force and velocity and the electrically induced force is  $F_e = b_e\dot{z}$ , the converted electrical power is:

$$P_e = \frac{1}{2}F_e\dot{z} = \frac{1}{2}b_e\dot{z}^2. \quad (3.2)$$

The magnitude of the output electrical power can be derived from Eq. (3.1) and Eq. (3.2) as [52]:

$$|P_e| = \frac{m\xi_e\omega_n\omega^2(\frac{\omega}{\omega_n})^3Y^2}{(2(\xi_e + \xi_m)\frac{\omega}{\omega_n})^2 + (1 - (\frac{\omega}{\omega_n})^2)^2}, \quad (3.3)$$

where  $Y$  is the displacement magnitude of input vibrations,  $\xi_e$  and  $\xi_m$  are the electrical and mechanical damping ratios, respectively;  $\omega$  is the input frequency and  $\omega_n$  is the natural frequency of the system. When the natural frequency of the system is matched to the input frequency, this expression is simplified as:

$$|P_e| = \frac{m\xi_e\omega^3Y^2}{4(\xi_e + \xi_m)^2}. \quad (3.4)$$

The generated power is maximized for  $\xi_e = \xi_m = \xi$ . Considering that  $f = \omega/2\pi$ , the Eq. (3.4) becomes:

$$|P_e|_{max} = \frac{\pi^3}{2} \frac{mf^3Y^2}{\xi}. \quad (3.5)$$

Several conclusions can be drawn from Eq. (3.5). The possible generated power heavily depends on the input frequency  $f$ . This frequency is, however, determined by the application of the energy harvester and its environment. Vibrations in the environment also determine the displacement magnitude  $Y$ . Furthermore, the generated power is linearly proportional to the mass. Finally, it is up to a device designer to minimize  $\xi_e$  and match it properly to  $\xi_m$  in order to obtain higher output power.

The described model and the estimated output power clearly indicate that the harvesting of the vibration energy inside the human body is a very challenging

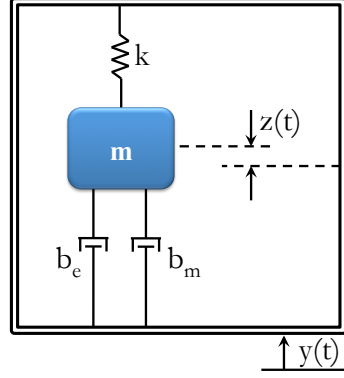


Figure 3.1: General model of vibration harvester [52].

task. First of all, the fundamental frequencies of the human motion are around 1 Hz, which severely limits the potential harvested power. Some recent measurements have showed that the spectral content of a moving person stretches up to tens of Hz [53], but the obtainable power at these frequencies is still very low. Second, a size and weight limitation of an implantable device restricts the value of the oscillating mass. Third, the actual movement of the human body is unpredictable and differs very much from person to person. It depends on person's age, health, mobility and many other factors. Also, the movement of the implantable device is influenced by the placement point inside the body. For instance, a device inside the patient's leg could potentially harvest much more power than a device inside the abdomen. Finally, the extracted power also depends on the used transduction mechanism.

As previously mentioned, there are three transduction mechanisms for converting the energy from vibrations to the electrical energy.

**Electromagnetic transducers** use the Faraday Law to convert the mechanical energy into electrical energy. The movement of a magnetic mass causes a variation of the magnetic flux in the nearby coil. This change in the magnetic generates an AC voltage across it. Generally, electromagnetic generators can achieve relatively high power densities, but at the cost of the device volume. This is because the harvested power depends on the number of windings in a coil, which is limited by the size of the device. Another disadvantage of this technique is that over time it is subject to a damage of the oscillating parts due to the constant movement and friction. This limits the lifetime of the harvester. Only a few miniature electromagnetic transducers with a relatively low operating frequency have been reported in the literature. In [54], a maximum output power of  $17.8 \mu\text{W}$  is obtained for WSN applications. The device is operating at 56.6 Hz and occupies  $150 \text{ mm}^2$ . This

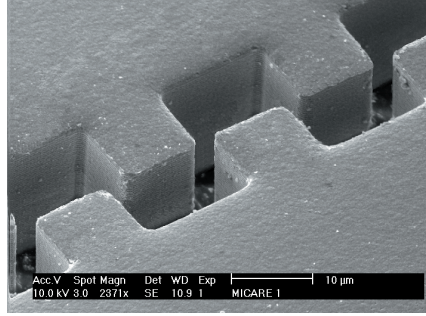


Figure 3.2: Comb-shaped capacitor for electrostatic energy harvesting [56].

result is equivalent to a power density of around  $100 \mu\text{W}/\text{cm}^3$ . In [55], an output power of  $43 \mu\text{W}$  at  $3.33 \text{ Hz}$  is obtained for implantable biomedical applications. The electromagnetic harvester, previously developed to power the quartz watches, have been implanted in a dog. The power density of this device is around  $10 \mu\text{W}/\text{cm}^3$ .

**Electrostatic transducers** utilize variable capacitors to convert the mechanical energy into electrical energy. When the distance or the overlap of the capacitor's plates is changed by motion or vibration, the voltage across the capacitor is also changed, and the electrical power is generated. The critical parameter of electrostatic transducers is the capacitance of a variable capacitor. To maximize this capacitance, many different fabrication techniques and shapes are used. The comb-like structure is shown in Fig. 3.2 [56]. Electrostatic energy harvesters are more efficient when they are generating small amounts of power. Their main advantage is that they are suitable for integration in microsystems and could be realized with MEMS. However, the capacitor needs to be pre-charged to operate properly. A very interesting electrostatic vibration energy transducer is presented in [56]. It is fabricated using MEMS fabrication technology, and it is the non-resonant device capable of operating at different frequencies. The reported frequency range is  $1 \text{ Hz} - 200 \text{ Hz}$ , and it can deliver  $12 \mu\text{W}/\text{cm}^2$ . Another interesting solution, presented in [57], is also fabricated using MEMS technology, and it is suitable for biomedical applications. This non-resonant device operates in the range  $1 \text{ Hz} - 100 \text{ Hz}$  and it can, theoretically, provide  $27 \mu\text{W}/\text{cm}^2$  at  $30 \text{ Hz}$ . However, in practice, the measured power density is around  $1 \mu\text{W}/\text{cm}^2$ .

**Piezoelectric transducers** are based on the properties of piezoelectric materials. When a piezoelectric material is exposed to mechanical stress, a voltage is generated across it. Unlike in electrostatic transducers, no pre-charge of the material is required in piezoelectric converters. The structure of a piezoelectric converter is shown in Fig. 3.3 [58]. The main disadvantage is that piezoelectric materials have a relatively high resonance frequency. Thus, they are not well suited to harvest en-

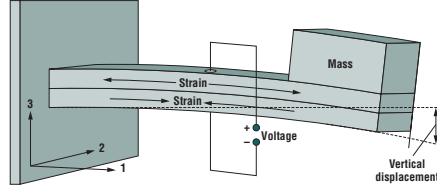


Figure 3.3: Piezoelectric energy harvester structure [58].

ergy from the low frequency human motion. In [59], the aluminium nitride (AlN) is used as piezoelectric material and a maximum power density of around  $60 \mu\text{W}/\text{cm}^3$  is measured at 572 Hz. A power density of around  $30 \mu\text{W}/\text{cm}^3$  at the relatively high frequency of 1500 Hz is reported in [60].

Commercial solutions for vibration energy harvesting exist for many different applications, such as industrial automation or rail monitoring [61, 62]. However, none of those solutions are suitable for low frequency micro-scale energy harvesting from the human motion.

Based on the previous discussion, among different mechanisms, electrostatic transducers show the most potential for powering implantable devices. They can obtain relatively high power density at a low movement frequency and can be realized with MEMS. It is also important to note that vibration energy harvesters are generally biocompatible since they can be hermetically sealed.

The output voltage of a vibration energy harvester is an AC voltage. So, it cannot be used to power CMOS circuits directly. Therefore, a vibration energy harvester requires a customized interface circuitry. A PMU, which contains a rectifier and a step-down converter, can be employed as an interface circuit. Since the harvested power is very low, the power transfer efficiency is the primary concern in the design of the PMU. The PMUs for low power vibration energy harvesting reaching 85% efficiency have been reported in the literature [36, 38, 63].

### 3.2.2 Thermal Energy Harvesting

Thermal energy harvesters convert the thermal energy, in the form of temperature difference, into electrical energy. This process is based on the Seebeck effect: two junctions made of dissimilar conductors and being exposed to different temperatures will establish an open circuit voltage in between them. The basic element of thermal energy harvesters is a thermocouple, which is illustrated in Fig. 3.4.

A thermocouple is composed of two semiconductor materials and metallic connections. Two semiconductor materials are P-type and N-type, respectively. Due to the temperature difference at the opposite sides of the materials, charge carriers are diffusing. All carriers, electrons and holes, are moving from the hot side toward the cold side. This is forming an electrical potential, and current flow if the circuit

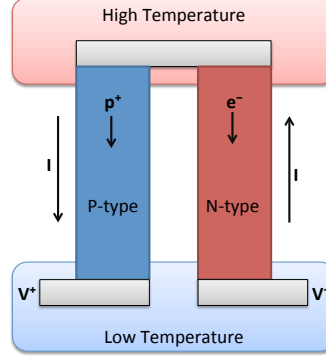


Figure 3.4: Thermocouple.

is closed. The established voltage is given by:

$$V = \alpha_1 \Delta T - \alpha_2 \Delta T, \quad (3.6)$$

where  $\alpha_1$  and  $\alpha_2$  are the material dependent Seebeck coefficients and  $\Delta T$  is the temperature difference between the opposite sides. Since the Seebeck coefficient of the N-type material is negative, contributions of both pillars in Eq. (3.6) are summed. The thermal energy harvester is made of a thermopile, which consists of many thermocouples connected together. From the thermal point of view, the thermocouples within the thermopile are connected in parallel and from the electrical point of view in series. If the number of thermocouples inside the thermopile is  $n$ , then the electrical parameters of the thermopile, the open circuit voltage  $V_T$  and internal resistance  $R_T$ , are given by:

$$V_T = n\alpha\Delta T, \quad (3.7)$$

$$R_T = 2n\rho\frac{h}{S}, \quad (3.8)$$

where  $\alpha$  is the sum of two Seebeck coefficients,  $\rho$  is the electrical resistivity of the materials (assumed to be equal for the simplicity),  $h$  is the height and  $S$  is the base area of the thermocouple legs (pillars). Consequently, the equivalent electrical model of the thermopile is very simple, as it is shown in Fig. 3.5(a). The obtained harvested power is derived as:

$$P_T = \frac{V_T^2}{4R_T} = \frac{n\alpha^2 S}{8\rho h} \Delta T^2. \quad (3.9)$$



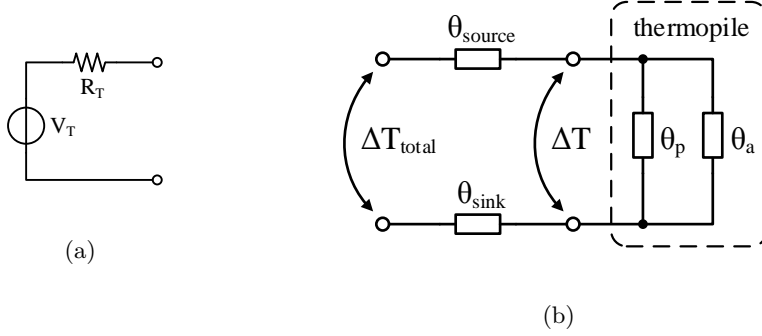


Figure 3.5: Equivalent models of a thermal energy harvester: (a) Electrical equivalent circuit, (b) Thermal model [65].

The Seebeck coefficient  $\alpha$ , the resistivity  $\rho$  and the ratio  $\frac{h}{S}$  of the pillars are defined by the technology and the used materials [28, 64]. The number of thermocouples inside the thermopile  $n$  can only be increased at the price of the area. Surprisingly, their number, within a specific area, is not maximized; it is rather set to an optimal value [28]. This is because there is an optimal density of thermocouples inside the thermopile for which the highest efficiency is obtained. To clarify the choice of the optimal number, the equivalent thermal model of the thermopile should be observed. The thermopile is modeled by two thermal resistors in parallel, as it is illustrated in Fig. 3.5(b) [65]. The thermal resistor  $\theta_p$  represents the thermal resistance of the pillars inside the thermopile and  $\theta_a$  is the thermal resistance of the air in between those pillars.  $\theta_{source}$  and  $\theta_{sink}$  represent the thermal resistances during heat exchange between the hot and the cold plate of the thermopile, and the environment, respectively. The actual temperature difference at the thermopile's plates  $\Delta T$  is lower than the temperature difference in the environment  $\Delta T_{total}$  and it is given by [65]:

$$\Delta T = \Delta T_{total} \frac{\theta_T}{\theta_T + \theta_{source} + \theta_{sink}}, \quad (3.10)$$

where  $\theta_T = \theta_p || \theta_a$  is the overall thermal resistance of the thermopile. In order to maximize  $\Delta T$ ,  $\theta_T$  must be maximized compared to sum  $(\theta_{source} + \theta_{sink})$ . It is known that [66]:

$$\theta_p = \frac{1}{k_p} \frac{h}{2nS}, \quad (3.11)$$

$$\theta_a = \frac{1}{k_a} \frac{h}{A - 2nS}, \quad (3.12)$$

where  $k_p$  and  $k_a$  are the thermal conductivities of the pillars and air in between them, respectively;  $A$  is the area of the thermopile's plate. To obtain the maximum

$\theta_T, \theta_p$  should be equal to  $\theta_a$ , therefore:

$$\frac{1}{k_p} \frac{h}{2nS} = \frac{1}{k_a} \frac{h}{A - 2nS}. \quad (3.13)$$

Eq. (3.13) defines the optimal number of thermocouples inside the thermopile for which the highest efficiency is achieved [28]:

$$n_{opt} = \frac{k_a}{k_a + k_p} \frac{A}{2S}. \quad (3.14)$$

There are two ways to additionally boost the output voltage and power of the thermopile [65]. First way is to further increase the thermal resistance of the thermopile by placing several devices thermally in series, which is equivalent to stacking them on top of each other. The drawback of this technique is an increased thickness of the resulting device. The second way is to decrease the sum ( $\theta_{source} + \theta_{sink}$ ) in Eq. (3.10) by a proper design of the thermopile's plates and outer surface.

The available temperature difference in a particular environment has to be defined before considering the powering from thermoelectric generators. In the case of implantable devices, this refers to the available temperature differences inside the human body. Since the human thermoregulatory system controls the core body temperature and keeps it at approximately 37 °C, the variations of the temperature inside the body are relatively low. The highest temperature gradient is available in the fat layer just under the surface of the skin [67, 68]. The temperature variation under the skin is shown in Fig. 3.6, where temperature differences up to 5 K can be seen in the fat layer. As it was explained above, the actual temperature difference between the plates of the energy harvesting device is much lower than in Fig. 3.6. Specifically, around 1 K - 2 K difference can be expected across the fat layer [68]. Such low temperature difference makes the thermal energy harvesting inside the human body extremely challenging.

Due to the limited temperature gradient inside the human body, the output voltage of the implantable thermal energy harvester is expected to be very low (few tens of mV) [68]. Thus, the harvester output cannot directly power the CMOS circuits. It requires a customized interface to boost the voltage to useful levels. Usually, a PMU with a special start-up capability and relatively high efficiency is employed, such as in [69].

The stacking of harvester devices thermally in series improves the effective temperature difference [64, 68], as it was already mentioned. In addition, if the devices are at the same time connected electrically in series, the output voltage is also increased. The drawback of this technique, i. e. the increased thickness, can serve as an advantage in implantable thermal energy harvesting [67]. A thicker device can exploit the total temperature difference across the fat layer of the human body effectively. Hence, instead of 1 K, entire 5 K of available difference can be used for harvesting. In Fig. 3.7, the comparison between the actual temperature differences on the harvester plates for a single and three stacked devices is shown [68]. The

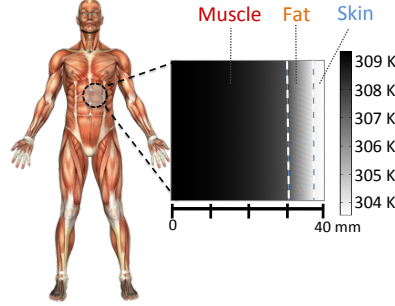


Figure 3.6: Modeled tissue temperature profile under the skin surface [67].

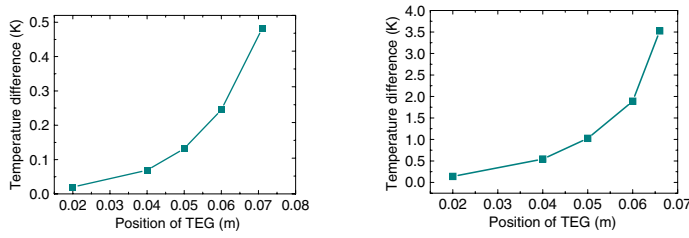


Figure 3.7: Comparison of temperature differences across a single and multiple TEGs [68].

comparison suggests that for thermal energy harvesting from the human body a few stacked devices are offering several advantages compared to a single device.

Currently, there are many commercially available thermo electrical energy harvesters, or so-called TEGs (Thermo-Electric-Generators), which are mostly intended for higher temperature differences [70–73]. ThermoLife company offers the TEG based on  $Bi_2Te_3$  which generates  $120 \mu W$  and  $2.9 V$  under the temperature difference of  $5 K$  and occupies an area of  $3 cm^2$  [70]. There is no information about the performance at lower temperature differences, but it can be extrapolated that the device would provide around  $5 \mu W/cm^2$  and  $20 mV/cm^2$  at  $1 K$  temperature difference. Another company named Nextreme [71] offers a tiny device ( $2.1 mm \times 3.4 mm$ ) which generates  $1 mW$  and  $180 mV$  at the temperature difference of  $10 K$ . Data is not available for lower values of temperature differences. Micropelt company offers a state-of-the-art device [73] which is only  $4.2 mm \times 3.4 mm$  in size and it generates  $15 \mu W$  at only  $1 K$  temperature difference, which corresponds to a power density of  $100 \mu W/cm^2$ . This means that three stacked devices from Micro-

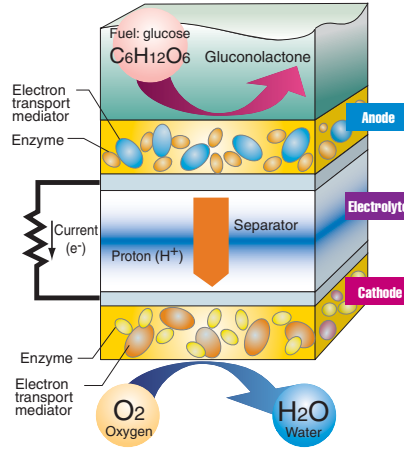


Figure 3.8: Glucose biofuel cell [74].

pelt inside the fat layer under the human skin can theoretically provide up to 130  $\mu W$ . It should be noted that these results are obtained from the simulations performed within the company, most probably in ideal conditions. The aforementioned thermal effects will result in relatively lower values in real applications.

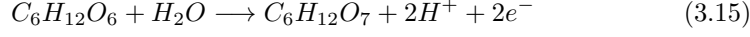
For use in implantable medical applications, the biocompatibility of TEGs must be considered. The main concern for thermal energy harvesters is the toxicity of used thermoelectric materials. At the moment, most of TEGs are using bismuth telluride as the thermoelectric material. This material has a relatively low toxicity, but it can cause some mild health effects [67]. To solve this issue, the device can be enclosed in a biocompatible material.

### 3.2.3 Biochemical Energy Harvesting

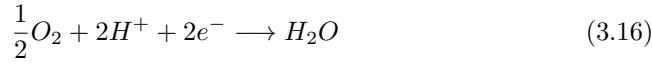
Biochemical energy harvesters, also called biofuel cells, convert the energy stored in chemical bonds into electrical energy. In medical implants, a biofuel cell generates the power by complementary chemical reactions at a pair of electrodes. Oxidation occurs at the anode electrode and reduction takes place at the cathode. Chemical reactions are accelerated by the participation of the catalyst. The difference between biofuel cells and classical batteries is that in biofuel cells the concentration of reactants is continually re-established by body fluids. Theoretically, this allows them to produce the electrical energy continuously.

Due to its omnipresence in body fluids, glucose is the most commonly used fuel

in biofuel cells. The glucose is oxidized at the anode [74]:



The residing hydrogen ions are passing through the protective membrane (separator). On the other hand, the electrons are blocked by the membrane and directed through an external load. This process is illustrated in Fig. 3.8. Afterwards, the reduction of oxygen is performed at the cathode, resulting in an overall charge neutrality [74]:



The water produced by the oxidation is also passing the membrane. Based on the catalyst that is used to speed up the reaction at the anode, the glucose biofuel cells can be classified into three groups: enzymatic fuel cells, microbial fuel cells and abiotic fuel cells.

**Enzymatic biofuel cells** are enzymatically catalyzed. This type of biofuel cells employs enzymes such as the glucose oxidase and laccase to accelerate chemical reactions. The enzyme-based biofuel cells provide high power densities up to  $100 \mu\text{W}/\text{cm}^2$  [75]. In [76], a miniature biofuel cell occupying only  $0.0026 \text{ mm}^2$  and providing  $4.3 \mu\text{W}$  of power is presented. In [77], this type of a biofuel cell is implanted in a rat, providing  $24.4 \mu\text{W}/\text{cm}^2$  for a few minutes. However, the enzyme-based biofuel cells suffer from a serious drawback. Their lifetime is quite short (can reach only a few months at present). Therefore, their usability is limited to applications that require only short-term powering.

**Microbial biofuel cells** are using living microorganisms to catalyse reactions at the anode. This type of fuel cells is very efficient and have a self-regenerative characteristic. The self-regeneration of the catalyst results in a theoretically unlimited lifetime. Their power density is also very high. The microbe-based fuel cells can produce around  $1000 \mu\text{W}/\text{cm}^2$  [78]. However, implanting the bacteria inside the body is unsafe for the patients. At the moment, this type of biofuel cells is far from being accepted as a biocompatible powering solution.

**Abiotic biofuel cells** are abiotically catalyzed. This kind of fuel cells utilizes non-organic catalyst such as noble metals or activated carbon. The power density of the abiotically catalyzed biofuel cells is limited to several  $\mu\text{W}$  and it is the lowest among all three types. On the other hand, unlike enzymatic ones, the abiotic biofuel cells can provide energy for many months [79]. The glucose biofuel cells, presented in [80] and shown in Fig. 3.9, can be fabricated using semiconductor fabrication techniques. Thus, these biofuel cells can be manufactured with the CMOS circuits on the same silicon wafer, but they are generating only  $3.4 \mu\text{W}/\text{cm}^2$ .

The output voltage of a miniature biofuel cell is also relatively low (a few hundreds of mV). Therefore, it also requires an interface circuitry (PMU) in order to provide the power and voltage levels needed for the CMOS circuits, such as in [41].

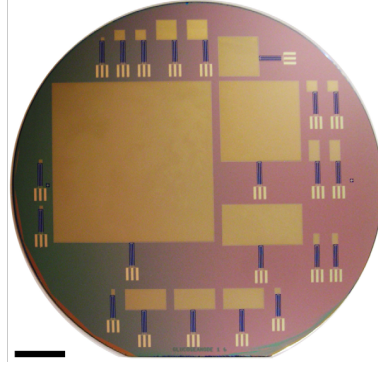


Figure 3.9: Fuel cells fabricated on silicon wafer [80].

### 3.2.4 Ambient RF Energy Harvesting

An ambient RF energy harvester converts the energy from microwaves into electrical energy. The condition is that the sources of these microwaves are not dedicated for this purpose, but they are rather a part of standard broadband infrastructures. These sources include AM and FM radio, TV broadcasting, cellular networks and Wi-Fi networks. It is immediately evident that the available power in the urban areas is much higher than in the rural areas.

Considering that the RF power source in the proximity is transmitting a signal with the power  $P_T$ , the theoretical received power is given by the Friis equation [81]:

$$P_R = P_T \frac{G_T G_R}{L_{path}}, \quad (3.17)$$

where  $L_{path}$  is the signal attenuation on the free space path,  $G_T$  and  $G_R$  are the gains of the transmitter and receiver antennas, respectively. It should be noted that this equation does not take into account any obstacles in the signal path. Therefore, the attenuation of the signal on its path mainly depends on the distance, and it is defined as:

$$L_{path} = \left(\frac{4\pi r}{\lambda}\right)^2, \quad (3.18)$$

where  $r$  is the distance from the transmitter and  $\lambda$  is the wavelength at the frequency of interest ( $\lambda = \frac{c}{f}$ ,  $c$  is speed of light). The distance from the transmitter is variable and depends on the location of the device. The transmitted power  $P_T$  and the gain of the transmitter antenna  $G_T$  are fixed. Once the targeted band is selected, the wavelength is also set. So, only the gain of the receiver antenna  $G_R$  can be manipulated. However,  $G_R$  depends strongly on the physical size of the antenna, which means that miniature antennas for implantable applications have a very low

gain. In addition, it is extremely challenging to design a miniature antenna for long wavelength bands, such as FM radio [82]. This limits the choice of bands to ones located at higher frequencies which experience higher signal attenuations. Therefore, the available ambient RF energy is very limited.

The achievable power density for medium size antennas is from  $0.2 \text{ nW/cm}^2$  to  $1 \text{ }\mu\text{W/cm}^2$  [82], which is quite low compared to other potential sources. In implantable devices, the signal is additionally attenuated by the surrounding human tissue and the size of the antenna is heavily limited. Therefore, the achievable power densities are expected to be even lower.

In order to be used for powering the CMOS circuits, the RF signal requires the RF to DC conversion. Due to the low input power, the efficiency of this conversion is usually less than 40%, which further limits the actual power that is available to power a device [82, 83].

### 3.3 Comparison and Discussion

The overall comparison of the different energy harvesting techniques for implantable biosensors is presented in Table 3.1. The potentially achievable energy densities and the crucial pros and cons of the various energy harvesters are emphasized.

The energy harvested from the human motion and vibrations can be utilized in biosensors since sufficient power levels can be obtained. However, due to the high resonant frequency and the damage over time of the moving parts, many existing solutions are not suitable for implantable biosensors. The viable solutions are limited by the strict weight and size requirements. In addition, during the periods of motion absence, e. g. during sleep, the energy harvester might provide insufficient power, which raises reliability issues since the obtained power is highly unpredictable.

Biochemical energy harvesting using glucose fuel cells is a feasible solution for powering implantable biosensors. However, among different types, only abiotically catalyzed biofuel cells can meet the requirements in terms of lifetime and biocompatibility. The concentration of glucose in cerebral fluid makes them particularly interesting for the applications related to monitoring brain neural activity. If the technological development is going to provide a higher power density, they may become the primary solution for such applications in the future.

Thermoelectric energy harvesting is also a viable solution. There is a temperature gradient within the human body, from which the energy can be harvested. However, due to the relatively low number of in vivo experiments, it is not clear how will the thermoelectric harvester behave in practice. The thermal matching might prove difficult and, consequently, results in much lower effective temperature difference over the device. Nevertheless, at the moment, thermoelectric harvesters provide superior power densities compared to other potential sources.

The energy density of RF ambient energy harvesting is the lowest among the overviewed energy sources. In addition, there are many challenges involved in

Table 3.1: Comparison of potential energy harvesting sources for implantable devices.

| Harvesting Technique                             | Type        | Power density<br>[ $\mu W/cm^2$ ] | Comments  |
|--|-------------|-----------------------------------|---|
| <b>Thermal</b><br>$\Delta T = 1 - 5K$<br>[70–73] | All         | 40 – 100                          | + High power density<br>+ Small size<br>+ Commercially available<br>– Thermal matching      |
| <b>Vibration</b><br>[54–57, 59, 60]              | Electromag. | 100                               | + High power density<br>+ Small size<br>+ Low operating frequency<br>– Damage over time     |
|  | Electrost.  | 12                                | + MEMS fabrication<br>+ Small size<br>+ Non resonant<br>– Capacitor pre-charging            |
|  | Piezoel.    | 60                                | + High power density<br>+ Small size<br>+ No capacitor pre-charging<br>– High frequency     |
| <b>Biochemical</b><br>[76–80]                    | Enzymatic   | 24.4                              | + High power density<br>+ Biocompatible<br>– Short lifetime                                 |
|  | Microbial   | 1000                              | + Very high power density<br>+ Long lifetime<br>– Not biocompatible                         |
|  | Abiotic     | 3.4                               | + Fabrication on silicon wafer<br>+ Long lifetime<br>+ Biocompatible<br>– Low power density |
| <b>RF Ambient</b><br>[82]                        | All         | < 1                               | – Very low power densities<br>– Miniature antenna design<br>– Low efficiency                |



designing the miniature, high-gain receiving antennas. The available energy exists, but it is low and not efficient to harvest. Additionally, the available RF energy heavily depends on whether the harvesting is performed in urban or rural locations.

The energy harvesting overview shows that, in many cases, only one of those sources is not enough. An alternative solution is to combine these individual sources into the multi-source energy harvesting. For instance, it is possible to use both thermoelectric and motion energy harvesting in parallel [38]. In fact, the multi-source energy harvesting is beneficial in terms of higher power and improved reliability. However, the system complexity increases while the overall power density remains similar. Following this idea, hybrid energy harvesting, in which the same device is capable of extracting the energy from different sources, appeared recently [84]. In [85], a simultaneous biochemical and motion energy harvester is presented.

Technology related to thermal energy harvesting is evolving rapidly. This is because the same technology is used for manufacturing the thermoelectric coolers (TECs) for the thermal management of microprocessor chips. There are two popular applications (TEG and TEC) of the similar technology, so many studies are focusing on thermoelectric technology. Consequently, commercially available thermal energy harvesters with promising performance have appeared. These harvesters can provide considerable power densities even at very low temperature differences, such as inside the human body. Finally, high power density, small size, unlimited lifetime, biocompatibility and ubiquitous temperature difference inside the human body makes thermal energy harvesting the most promising solution for many implantable biosensor applications.



## Chapter 4

# Power Management Unit

A thermoelectric energy harvester, implanted in the human body, provides very low output voltage and power, which are variable and unpredictable at the same time. Therefore, the resulting output voltage, during some periods, might be as low as tens of mV and the resulting power a few  $\mu\text{W}$ . On the other hand, implantable biosensor circuits require stable voltage supplies, for instance 1.8 V, and might consume a few mW of power. The power management unit (PMU) corrects for these differences and enables a thermoelectric energy harvesting to power the biosensor circuits. It converts the low voltage from the energy harvester to the voltage or multiple voltages required by the biosensor circuits. In addition, it manages energy transfers from the energy harvester to the storage device and further to the biosensor circuits. These transfers have to be highly efficient so that as little energy as possible is lost. The high efficiency is extremely hard to obtain considering that the input power is very low, and the voltage conversion ratio is high. For this reason, all potential losses within the PMU and the power consumption of the control circuitry have to be minimized.

The simplified block diagram of the PMU is shown in Fig. 4.1. The PMU serves as an interface between the energy harvester, the energy storage, and the biosensor circuits. The main tasks of the PMU are performed by the input converter, which converts the input voltage and transfers the energy from the input to the storage device. The start-up block is responsible for pre-charging the storage device so that the initial voltage is sufficient for the proper functionality of the circuits. The storage monitor observes the voltage of the storage device and informs the biosensor when there is enough energy accumulated for entering the active state. Finally, the voltage regulator provides the stable supply voltages to the biosensor circuits.

The input converter is the key block of the PMU, it defines the functionality and efficiency of the PMU, and because of this, it is the main focus of this chapter. First of all, the input converter architecture is proposed. Then, the sources of losses within the converter are analyzed in detail. Further, the design procedure of the proposed input converter for minimizing these losses is defined. Finally, the

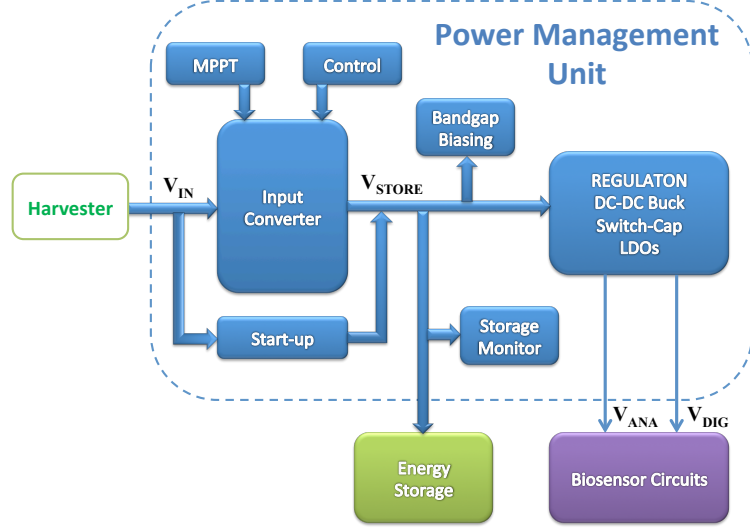


Figure 4.1: Block diagram of the PMU.

additional tasks of the PMU, such as the maximum power extraction (MPE) and successful start-up, are addressed. The low power control of the input converter will be covered in the next chapter.

#### 4.1 Input Step-up Converter Design

Based on the requirements of the PMU and limitations of the complete implantable system described in the previous chapters, the most important features of the input converter can be identified as: the efficient conversion and the small size. Unfortunately, these two key features are trading-off with each other. Generally, the boost converters with external inductors obtain the high voltage conversion efficiency at the cost of necessary external components, so their scaling is somewhat limited. On the other hand, the switched-capacitor step-up converters (or so-called charge pumps) can be fully integrated and miniaturized, but their efficiency is usually lower than that of the inductive boost converters.

Recent technology advancements and circuit development have enabled switched-capacitor converters to reach higher efficiencies. In the ideal case, the efficiency is determined by the conduction losses, which are proportional to the difference ( $MV_{in} - V_{out}$ ), and the switching losses are not taken into account. Therefore, the

theoretical efficiency of the switched-capacitor converter is given as [86]:

$$\eta_{theoretical} = \frac{V_{out}}{MV_{in}} \quad (4.1)$$

where  $V_{in}$  and  $V_{out}$  are the input and output voltages, respectively, and  $M$  is the conversion ratio. The obtained efficiency might be relatively high if  $V_{out}$  is close to the product  $MV_{in}$ , but this condition is very difficult to satisfy in applications where  $V_{in}$  or  $V_{out}$  or both are varying in a wide range [86]. For this reason, most of the efficient switched-capacitor converters have a fixed conversion ratio [87–90]. This problem might be solved, up to some extent, by using a multi-ratio approach, where  $M$  is constantly changed to improve the efficiency [40, 91, 92]. Once  $M$  is set, in real cases, the efficiency is further reduced by switching losses. The two primary sources of switching losses are bottom-plate losses due to the parasitics of floating capacitors and driver losses related to the power consumption of switch drivers. Unfortunately, as the required number of different possible ratios increases, more and more switches and drivers are necessary, which limits the overall efficiency improvement and increases the system size [93]. For example, in the state-of-the-art work [40], the minimum input voltage of 600 mV is converted to 1.8 V using three different conversion ratios (the maximum ratio is also three) with the overall conversion efficiency of 70%. In this design MIM capacitors with very low parasitics are used and the resulting area is relatively large, approximately 60 mm<sup>2</sup>.

In thermoelectric energy harvesting applications, both the input and output voltages are varying, so they require a multi-ratio approach. The input voltage can be lower than 40 mV, and the output voltage is around 1.8 V leading to a maximum conversion ratio higher than 40. To obtain such high conversion ratio, at least nine floating capacitors are necessary [93]. The resulting number of switches, for distributing the charges between nine floating capacitors and adjusting the conversion ratio at the same time, is very high. Controlling and driving these switches is a power consuming task. Moreover, a high number of capacitors results in significant bottom-plate losses. For these reasons, the resulting efficiency of potential switched-capacitor solutions is expected to be unacceptably low.

On the other hand, the efficiency of inductive boost converters does not directly depend on the conversion ratio, so the high efficiency is achievable even for very high conversion ratios [86]. Additionally, the complexity is not drastically increased if the multi-ratio operation is introduced. External components, of course, increase the overall area and the cost of the power management subsystem. To keep the number of external components as low as possible, a regular boost topology with only one inductor can be used. This topology can potentially meet the severe performance requirements dictated by the target application. In fact, similar topologies are used in most of the related work [35, 37, 39, 69, 94–97]. However, many design challenges exist, which become more drastic when the PMU is dedicated to energy harvesting applications. Particularly, different loss mechanisms and the power consumption of the control circuits are limiting the conversion efficiency. Taking into consideration that the input power is extremely low, every nW of losses or consumed in the

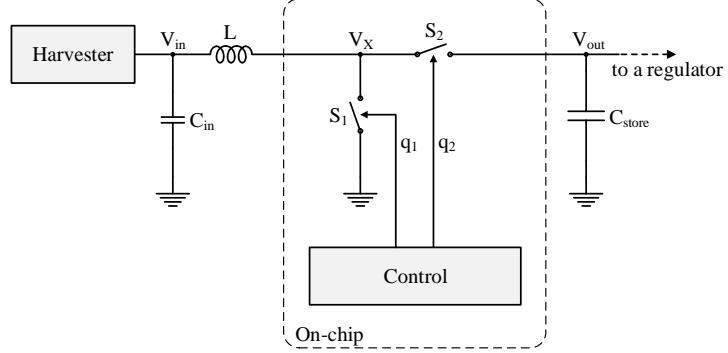


Figure 4.2: Simplified schematic of the boost converter.

control influences the overall efficiency. These problems will be addressed later in this chapter. It is also important to note that the solutions with integrated inductors do not offer any advantage over switched-capacitors approaches [98].

A boost converter with an external inductor provides a superior performance when high and variable conversion ratio is required [86]. Therefore, such converter, as it is shown in Fig. 4.2, is used in this work. Since it is processing a low input power, the converter is operating in the discontinuous conduction mode (DCM). This means that the current is not continuously flowing through the inductor, but it is equal to zero during some parts of the cycle. To briefly describe the operation of the boost converter, its full cycle can be divided into three sections according to the state of the switches: i) when the switch  $S_1$  is ON and the switch  $S_2$  is OFF, the energy is accumulated over the inductor; ii) when the switch  $S_1$  is OFF and the switch  $S_2$  is ON, the energy is transferred from the inductor to the output capacitor; iii) when both switches are OFF, the converter is basically in the idle state, waiting for the next cycle.

The detailed operation of the boost converter is illustrated in Fig. 4.3. Considering  $t_0$  as an initial point, first, the switch  $S_1$  is turned-on and the resulting voltage across the inductor,  $V_{in}$ , slowly builds up the current in the inductor according to the following expression:

$$i_L(t) = i_L(t_0) + \frac{1}{L} \int_{t_0}^t V_{in} dt = \frac{V_{in}}{L} (t - t_0), \quad t_0 \leq t \leq t_1, \quad (4.2)$$

where  $L$  is the inductance of the external inductor. If the switch  $S_1$  is turned-off at the moment  $t_1$ , then the maximum inductor current is given by:

$$i_L(t_1) = \frac{V_{in}}{L} (t_1 - t_0) = I_{L,max}. \quad (4.3)$$

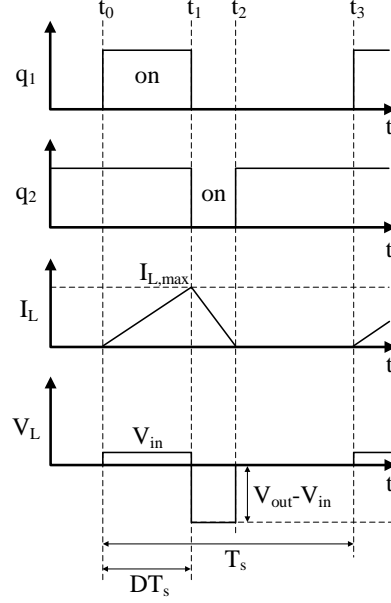


Figure 4.3: Switching diagram of the boost converter.

At this point, the energy accumulated in the inductor is:

$$E_{ind,max} = \frac{1}{2} L I_{L,max}^2. \quad (4.4)$$

Afterwards, the switch  $S2$  turns-on and assuming that the output voltage is already established to  $V_{out}$ , the voltage across the inductor becomes  $(V_{in} - V_{out})$ . The accumulated energy is transferred to the output capacitor [69], and the inductor current is decreasing as:

$$i_L(t) = I_{L,max} - \frac{V_{out} - V_{in}}{L}(t - t_1), \quad t_1 \leq t \leq t_2. \quad (4.5)$$

To obtain the steady state operation of an ideal boost converter, the energy stored in the inductor has to be the same at the beginning and the end of the period [99]. This means that the currents through the inductor have to be the same. In this particular case, the initial current through the inductor was equal to zero, so the final current should also be equal to zero:

$$i_L(t_2) = I_{L,max} - \frac{V_{out} - V_{in}}{L}(t_2 - t_1) = 0. \quad (4.6)$$

From Eq. (4.3) and (4.6), the condition for the proper functionality of the boost converter can be obtained:

$$\frac{V_{in}}{t_2 - t_1} = \frac{V_{out} - V_{in}}{t_1 - t_0}. \quad (4.7)$$

The same condition can be obtained by following the inductor volt-second balance (IVSB), which states that for the steady state operation, the average voltage across the inductor in a switching period must be zero [99].

It can be concluded that when Eq. (4.7) is satisfied, the converter operates in the steady state and transfers, in every cycle,  $E_{ind,max}$  to the load. Substituting Eq. (4.3) into Eq. (4.4) yields:

$$E_{ind,max} = \frac{V_{in}^2(t_1 - t_0)^2}{2L}. \quad (4.8)$$

If the operating period of the converter is  $T_s$  (and frequency  $f_s$ ), the duration of the switch  $S1$  ON time ( $t_1 - t_0$ ) can be expressed as  $DT_s$ , where  $D$  is the duty ratio of the converter. Therefore, Eq. (4.8) becomes:

$$E_{ind,max} = \frac{V_{in}^2(DT_s)^2}{2L}. \quad (4.9)$$

The output power can be calculated as:

$$P_{out} = E_{ind,max}f_s = \frac{1}{2}LI_{L,max}^2f_s = \frac{V_{in}^2D^2}{2Lf_s}. \quad (4.10)$$

In the traditional applications of the inductive boost converters, such as a switched-mode power supply (SMPS), the output power is adjusted by tuning the duty ratio (pulse width modulation - PWM) or frequency (pulse frequency modulation - PFM) to support the power requirements of the load [99]. In the energy harvesting applications, since the obtainable power is limited by the source and, even if it is maximized, it is still too low to power the load, i. e. biosensor circuits, duty ratio (or frequency) tuning is not used [69, 95, 97]. Instead, the maximum possible power is provided at any time, as it will be seen later in this chapter.

The conversion efficiency of the boost converter is defined as [99]:

$$\eta = \frac{P_{out}}{P_{in}}, \quad (4.11)$$

where  $P_{in}$  is the average input power of the converter and  $P_{out}$  is the average output power delivered to the load. The analysis above is for an ideal boost converter, so the conversion efficiency,  $\eta$ , is equal to 100%, meaning that the entire power extracted from the source is provided to the load. In reality, the losses within the converter,  $P_{loss}$ , and the power consumption of its control circuits,  $P_{control}$ , are limiting the efficiency by decreasing the output power as [35, 99]:

$$P_{out} = P_{in} - P_{loss} - P_{control}, \quad (4.12)$$



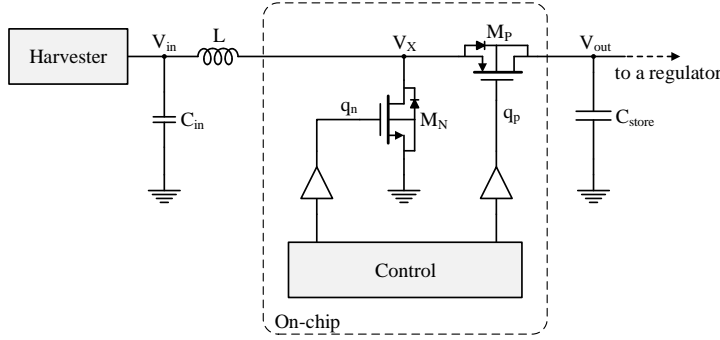


Figure 4.4: Boost converter schematic.

So, the conversion efficiency can be rewritten as:

$$\eta = 1 - \frac{P_{loss} + P_{control}}{P_{in}}. \quad (4.13)$$

It is evident from Eq. (4.13) that the sum  $(P_{loss} + P_{control})$  have to be reduced as much as possible compared to  $P_{in}$  in order to achieve high efficiency. This is especially problematic when the extracted power is very low, as it is in energy harvesting applications, where it can be less than  $5 \mu\text{W}$ . In such applications, special attention has to be taken to suppress all potential losses and to limit the power consumption of the control circuits.

## 4.2 Loss Mechanisms

The schematic of the boost converter, where switches are implemented with the transistors  $M_N$  and  $M_P$ , is shown in Fig. 4.4. The losses within the converter can be roughly divided into three categories:

- **Conduction losses**, which are related to parasitic resistances inside the converter. The most significant resistances include the inductor series resistance,  $R_L$ , the ON resistances of the switches,  $R_N$  and  $R_P$ , and the equivalent series resistance (ESR) of the output capacitor,  $R_{ESR}$ , as it is shown in Fig. 4.5. There are also other losses, such as parasitic resistances of wires and interconnects.
- **Switching losses**, which are associated with the undesired capacitances within the converter. The most significant switching losses are switch driver losses necessary to turn the switches ON and OFF. However, other nodes may also introduce switching losses.

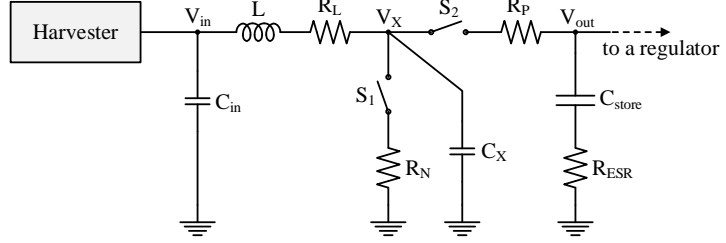


Figure 4.5: Schematic of a boost converter with parasitics.

- **Synchronization losses**, which originate from inaccurate switching timings when the switch  $M_P$  (pFET) turns ON and OFF too late or too early.

The following sections will address these categories individually. Particular attention will be given to synchronization losses, which become significant as the input power approaches very low levels.

#### 4.2.1 Conduction Losses

The conduction losses of a particular parasitic resistor are defined by [86]:

$$P_{cond,i} = I_{rms,i}^2 R_i, \quad (4.14)$$

where  $I_{rms,i}$  is the root mean square (RMS) current which is flowing through the resistance  $R_i$ . The conduction losses related to the nFET switch,  $M_N$ , can be estimated by using Eq. (4.14):

$$P_{cond,N} = I_{rms,N}^2 R_N, \quad (4.15)$$

where  $R_N$  is the ON resistance of the transistor  $M_N$ . The RMS current through  $M_N$  can be expressed as:

$$I_{rms,N} = \sqrt{\frac{1}{T_s} \int_0^{T_s} i_N^2(t) dt}. \quad (4.16)$$

When the transistor  $M_N$  is conducting ( $t_0 \leq t \leq t_1$ ), its current is equal to the inductor current and it is defined by Eq. (4.2), otherwise, it is equal to zero. If the duration of  $M_N$  ON time is  $\tau_N = t_1 - t_0$ , then the Eq. (4.16) can be rewritten as:

$$I_{rms,N} = \sqrt{\frac{1}{T_s} \int_0^{\tau_N} \frac{V_{in}^2}{L^2} t^2 dt} = \sqrt{\frac{V_{in}^2 \tau_N^3}{3L^2 T_s}}. \quad (4.17)$$

Combining Eq. (4.3), (4.15) and (4.17),

$$P_{cond,N} = \frac{V_{in}^2 \tau_N^3}{3L^2 T_s} R_N = \frac{I_{L,max}^2}{3} R_N \tau_N f_s. \quad (4.18)$$

The conduction losses related to  $M_P$  ON resistance,  $R_P$ , is similarly determined by:

$$P_{cond,P} = \frac{I_{L,max}^2}{3} R_P \tau_P f_s. \quad (4.19)$$

The conduction losses related to the series resistance of the inductor,  $R_L$ , can be written as:

$$P_{cond,L} = \frac{I_{L,max}^2}{3} R_L (\tau_N + \tau_P) f_s. \quad (4.20)$$

Eq. (4.18), (4.19) and (4.20) show that, as the input power is scaled down, the conduction losses are also scaled in the similar manner, and their influence on the overall efficiency remains almost the same. For example, since the input power is given as:

$$P_{in} = E_{ind,max} f_s = \frac{1}{2} L I_{L,max}^2 f_s, \quad (4.21)$$

the conduction losses related to the ON resistance of  $M_N$  can be expressed as:

$$P_{cond,N} = \frac{2P_{in}}{3L} R_N \tau_N, \quad (4.22)$$

where the relation between the transferred power and the conduction losses is evident.

#### 4.2.2 Switching Losses

The switching losses related to driving the gates are given by [86]:

$$P_{sw,i} = C_i V_i^2 f_s, \quad (4.23)$$

where  $C_i$  is the total gate capacitance,  $V_i$  is the high voltage level during switching and  $f_s$  is the switching frequency. Considering Eq. (4.23), the switching losses related to  $M_N$  and  $M_P$  can be estimated as:

$$P_{sw,N} = C_N V_{out}^2 f_s, \quad (4.24)$$

$$P_{sw,P} = C_P V_{out}^2 f_s. \quad (4.25)$$

The switching losses are not scaling with the transferred power. Therefore, at low power levels, switching losses might prevail over conduction losses. However, they can be reduced by decreasing the switching frequency or the size of the switches at the cost of higher conduction losses. The optimal switch sizes and switching frequency for which the overall sum of conduction and switching losses is minimized will be addressed in the section 4.3.

The nodes with the high parasitic capacitances can also introduce significant switching losses. The most critical such node is X in Fig. 4.5, since both switches,  $M_N$  and  $M_P$ , contribute to the total capacitance at this node, together with other contributors. In particular, as this node is connected to an external inductor, the parasitic capacitances from the metal traces of on-chip and off-chip interconnections, as well as from the pad, bond wire and leads are all summed up at this node. The switching losses related to the node X are given by [97]:

$$P_{sw,X} = \frac{1}{2} C_X V_{out}^2 f_s, \quad (4.26)$$

where  $C_X$  is the total parasitic capacitance at the node X.

In low power applications, the switch sizes and, consequently, the capacitances  $C_N$  and  $C_P$  are usually scaled down to reduce the gate driving losses. However, the capacitance  $C_X$  is not scaled down in the same way and, as a result, the switching losses related to the node X might become comparable to the gate driving losses.

### 4.2.3 Synchronization Losses

In boost converters operating in DCM, the synchronization losses completely depend on the timings of the pFET switch,  $M_P$ . More precisely, after  $M_N$  turns-off, the accurate time has to pass before  $M_P$  switch turns-on. Similarly, the duration of  $M_P$  ON time has to be accurate, so  $M_P$  should be turned-off again at a precise moment of time [100, 101]. Therefore, synchronization losses can be classified into two groups: A) losses related to  $M_P$  turn-off timing and B) losses related to  $M_P$  turn-on timing. The losses related to turning-off  $M_P$  are usually more significant and their impact is more often recognized.

#### A) Turn-off timing losses of the pFET switch

The turn-off timing of the pFET switch,  $M_P$ , defines the duration of its ON time ( $\tau_P$ ), as it is shown in Fig. 4.6. Three different scenarios can be distinguished [101]:

- **$\tau_P$  is accurate** – this means that  $M_P$  is turned-off in the right moment, as it is shown in Fig. 4.6(a). As it has been mentioned,  $M_P$  transfers the energy from the inductor to the output. Since the voltage across the inductor is negative during that process, the current in the inductor and through the switch is decreasing according to Eq. (4.5). In the ideal case,  $M_P$  should turn-off when this current reaches zero and if it does so no synchronization losses are introduced. This scenario is called Zero-Current Switching (ZCS).

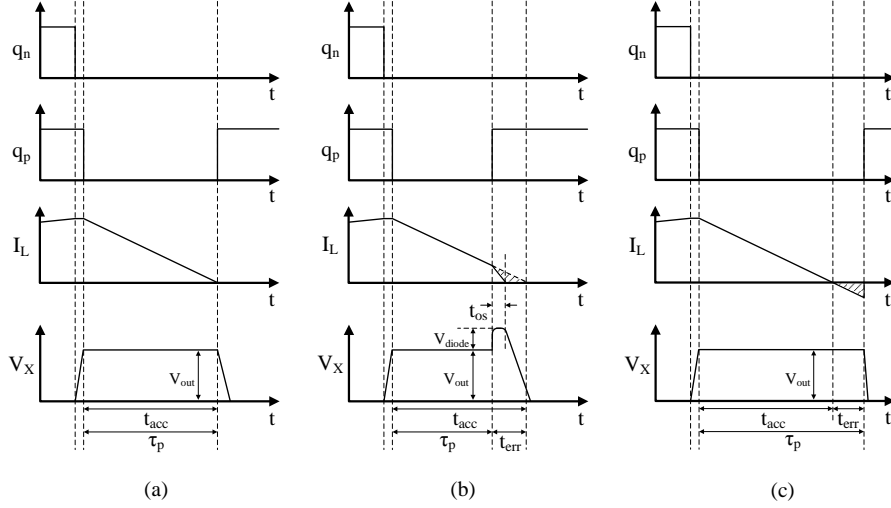


Figure 4.6: Detailed switching diagram during the pFET ON time [35].

- **$\tau_P$  is short** – this means that  $M_P$  is turned-off early, as it is illustrated in Fig. 4.6(b). Even though the transistor is off, the inductor current will continue to flow through the body diode of the transistor. The resistance of this forward-biased body diode is higher than the ON resistance of  $M_P$ , so additional losses are introduced. As closer the  $\tau_P$  is to the accurate value, less losses are introduced. These losses can be approximated by observing the waveforms of the current through  $M_P$  shown in Fig. 4.6(b). Assuming that the output voltage during the duration of the error time  $t_{err}$  is constant, the lost energy is equivalent to the shaded area in Fig. 4.6(b) [35]:

$$E_{sync,short} = \frac{1}{2} V_{out} I_{L,max} \frac{t_{err}}{\tau_P} (t_{err} - t_{os}), \quad (4.27)$$

where  $t_{os}$  is the overshoot time that is illustrated in Fig. 4.6(b).

- **$\tau_P$  is long** – this means that  $M_P$  is turned-off late, as it is shown in Fig. 4.6(c). After reaching zero, the current through the inductor changes polarity and starts discharging the output capacitor. This means that the transferred energy is returned to the inductor and lost. This scenario is particularly problematic since it introduces relatively high losses and it should be avoided if possible. As closer the  $\tau_P$  is to the accurate value, the related losses are

lower. These losses can be approximated in similar way as in Eq. (4.27) [35]:

$$E_{sync,long} = \frac{1}{2} V_{out} I_{L,max} \frac{t_{err}}{\tau_P} t_{err}. \quad (4.28)$$

The overshoot time  $t_{os}$  is usually very close to the error time  $t_{err}$ . Taking this into account, it is evident from Eq. (4.27) and (4.28) that the losses related to long  $\tau_P$  are more significant.

### B) Turn-on timing losses of the pFET switch

In DCM operating converters, after  $M_N$  turns-off, it is necessary that a certain amount of time passes before  $M_P$  turns-on. This time is called dead time and it is preventing the situation in which both switches are conducting at the same time [100]. Otherwise, a low resistance path from the output to the ground is established, which would discharge the output capacitor and severely reduce the efficiency or even disturb the functionality. However, even when the dead time is introduced, depending on its duration, significant losses may endure. The dead time is basically defined by the moment in which  $M_P$  turns-on and three different scenarios can be distinguished as it is shown in Fig. 4.7 [101]:

- **Dead time is accurate** – this means that  $M_P$  is turned-on in the right moment, as it is shown in Fig. 4.7(a). When both switches are OFF, the inductor current is charging the parasitic capacitance at node X. If  $M_P$  is turned-on at the same moment when this capacitor is charged to the value of the output voltage, the almost lossless switching is achieved. In other words,  $M_P$  should be turned-on when  $V_X = V_{out}$ . This scenario is called Zero-Voltage Switching (ZVS).
- **Dead time is short** – this means that  $M_P$  is turned-on early, as it is illustrated in Fig. 4.7(b). In this situation, the voltage at node X is still lower than the output voltage,  $V_X < V_{out}$ , and it gets charged from the output capacitor. This reverse current flow is returning the already transferred energy and it is highly undesirable because it introduces significant losses.
- **Dead time is long** – this means that  $M_P$  is turned-on late, as it is shown in Fig. 4.7(c). Consequently, the voltage at node X exceeds the output voltage,  $V_X > V_{out}$ . Eventually, the body diode of  $M_P$  becomes forward-biased and starts conducting. The conduction losses of the body diode are higher than of the ON switch and additional losses are introduced.

As it will be shown, the accurate dead time depends on the conversion ratio of a boost converter, and in the applications where the conversion ratio is varying, the accurate dead time is also varying. Therefore, the dead time has to be adaptive to eliminate the dead time losses successfully. Nevertheless, usually, the dead time is set to a fixed duration and the related losses are neglected. For these reasons,

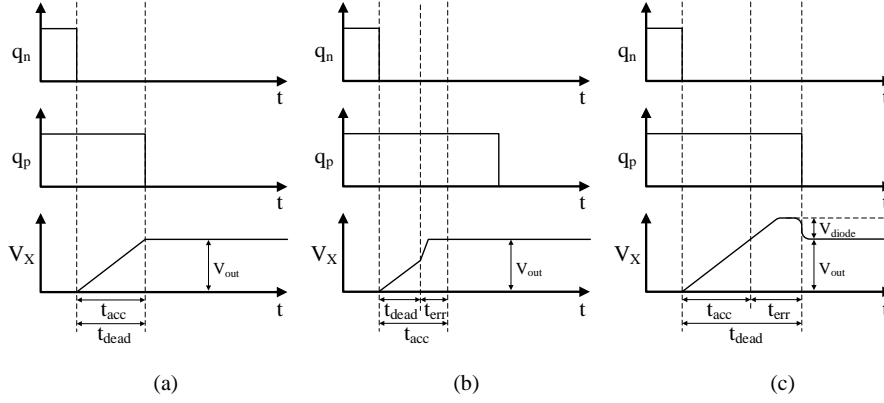


Figure 4.7: Detailed switching diagram during the dead time.

the detailed analysis of dead time losses is carried out in this work. The goals are to define the accurate dead time, to identify the consequences if the dead time is not accurate and to estimate the related losses and their influence on the overall efficiency.

The equivalent circuit of the boost converter during the dead time is shown in Fig. 4.8 [102]. The switches are OFF and can be represented as their corresponding body diodes. During the dead time, the inductor is acting as a current source providing the current equal to  $I_{L,max}$ . As it was already mentioned, the capacitance  $C_X$  incorporates all parasitic capacitances at this node and it is given by:

$$C_X = C_{jN} + C_{ovN} + C_{jP} + C_{ovP} + C_{par}, \quad (4.29)$$

where  $C_{jN}$  and  $C_{jP}$  are the depletion capacitances of the reverse biased  $M_N$  and  $M_P$  body diodes respectively,  $C_{ovN}$  and  $C_{ovP}$  are the overlap and fringing capacitance of turned-off transistors and  $C_{par}$  represents the sum of parasitic capacitances at the node X. The capacitance  $C_{par}$  includes the on-chip parasitic capacitance of metal interconnections, the capacitance of the pads, bondwires, leads, off-chip board capacitance, inductor parasitic capacitance, etc. The depletion capacitances are given by:

$$C_j = \frac{C_{j0}A}{\sqrt{1 + \frac{V_R}{\Phi_0}}}, \quad (4.30)$$

where  $C_{j0}$  is the depletion capacitance per unit area when  $V_R = 0$ ,  $A$  is the depletion region area,  $V_R$  is the reverse-bias voltage of the diode and  $\Phi_0$  is the built-in junction potential. It can be concluded from Eq. (4.29) and (4.30) that the depletion capacitances and, consequently, the capacitance  $C_X$  depend on the voltage

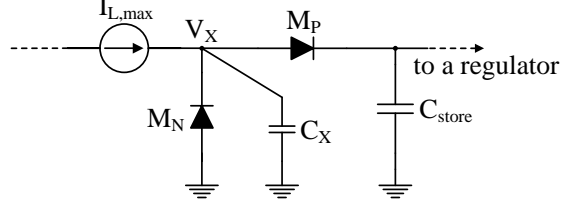


Figure 4.8: Equivalent circuit of the boost converter during the dead time [102].

$V_X$ . However, as  $C_{jN}$  decreases with  $V_X$ , and  $C_{jP}$  increases with  $V_X$ , their sum remains almost constant. In addition, the other capacitances contributing to  $C_X$  in the Eq. (4.30) do not depend on the voltage  $V_X$ . Therefore, the overall variation of the capacitance  $C_X$  due to the varying  $V_X$  is relatively low and can be considered almost constant in most cases [102].

According to the Fig. 4.8, during the dead time, the constant current  $I_{L,max}$  is charging the capacitor  $C_X$ . Therefore, the voltage  $V_X$  can be written as:

$$V_X(t) = V_X(0) + \frac{I_{L,max}}{C_X}t. \quad (4.31)$$

Assuming that the capacitor is completely discharged after  $M_N$  turns-off and that the accurate dead time is achieved when  $V_X = V_{out}$ , then:

$$\frac{I_{L,max}}{C_X}t_{acc} = V_{out}. \quad (4.32)$$

Combining Eq. (4.32) and (4.3) the accurate dead time,  $t_{acc}$ , can be estimated as:

$$t_{acc} = \frac{C_X V_{out}}{I_{L,max}} = \frac{C_X L}{\tau_N} \frac{V_{out}}{V_{in}} = \frac{C_X L}{\tau_N} K, \quad (4.33)$$

where  $\tau_N$  is the ON time of  $M_N$  and  $K = \frac{V_{out}}{V_{in}}$  is the conversion ratio of the converter. Furthermore, the steady-state condition, given by Eq. (4.7), can be rewritten as:

$$\frac{V_{in}}{\tau_P} = \frac{V_{out} - V_{in}}{\tau_N}. \quad (4.34)$$

Considering Eq. (4.34), for  $V_{out} \gg V_{in}$  the conversion ratio is approximately  $K \approx \frac{\tau_N}{\tau_P}$ . Finally, the accurate dead time can be expressed as:

$$t_{acc} \approx \frac{C_X L}{\tau_P}. \quad (4.35)$$



The duration of  $M_N$  ON time ( $\tau_N$ ) is usually fixed to achieve the MPE, so the duration of  $M_P$  ON time ( $\tau_P$ ) is varying to meet the condition (4.34) [69, 95, 97]. Consequently, the accurate dead time is also changing according to the levels of the input and output voltage. This means that in order to suppress the dead time losses, an adaptive dead time following the expression (4.35) at any moment, has to be used. However, usually a fixed dead time is used. In this case, to reduce the losses, a fixed dead time should be equal to the maximum possible value of the Eq. (4.35). As a result, the short dead time, which introduces significant losses, is avoided, but the dead time is longer than necessary and the body diode is conducting for a short duration almost every cycle. The related losses,  $P_{loss,dead}$ , can be estimated as [101]:

$$P_{loss,dead} = V_{diode} I_{L,max} t_{err} f_s, \quad (4.36)$$

where  $V_{diode}$  is the voltage drop of  $M_P$  body diode and  $t_{err}$  is the dead time error. As it can be seen from Fig. 4.7, the dead time error is  $t_{err} = t_{fix} - t_{acc}$ , where  $t_{fix}$  is the adopted fixed dead time and  $t_{acc}$  is the accurate dead time. Inserting Eq. (4.33) and (4.3) into Eq. (4.36), the losses can be written as:

$$\begin{aligned} P_{loss,dead} &= V_{diode} \frac{V_{in}}{L} \tau_N \frac{C_X L}{\tau_N} (K_{max} - K) f_s \\ &= V_{diode} V_{out} C_X f_s \left( \frac{K_{max}}{K} - 1 \right). \end{aligned} \quad (4.37)$$

If the output voltage is considered constant, the Eq. (4.37) can be rewritten as:

$$P_{loss,dead} = V_{diode} V_{out} C_X f_s \left( \frac{V_{in}}{V_{in,min}} - 1 \right). \quad (4.38)$$

According to Eq. (4.38), the dead time related losses will be the highest for  $V_{in} = V_{in,max}$ . The ratio  $\frac{V_{in,max}}{V_{in,min}}$  can easily reach values higher than 10 in many applications [27, 28], resulting in considerable losses. The expression (4.38) can be used to quickly estimate the dead time losses. In addition, the overall efficiency reduction,  $\Delta EFF$ , due to the dead time losses can be also estimated as:

$$\begin{aligned} \Delta EFF &= \frac{P_{loss,dead}}{P_{in}} \\ &= \frac{V_{diode} V_{out} C_X f_s \left( \frac{K_{max}}{K} - 1 \right)}{\frac{V_{in}^2}{R_{in}}} \\ &= \frac{V_{diode} R_{in} C_X f_s \left( \frac{K_{max}}{K} - 1 \right) K^2}{V_{out}}, \end{aligned} \quad (4.39)$$

where  $R_{in}$  is the input resistance of the boost converter. The efficiency reduction reaches its maximum for  $K = \frac{K_{max}}{2}$  and it is equal to:

$$\Delta EFF_{max} = \frac{V_{diode} R_{in} C_X f_s K_{max}^2}{4 V_{out}}. \quad (4.40)$$

Using the expression (4.40), the overall efficiency reduction due to the dead time losses can be easily estimated. All parameters are usually known in the initial phases of the converter design and only the capacitance  $C_X$  have to be extracted or estimated from the particular design. The efficiency reduction can easily exceed a few percentages, especially in the applications where the maximum conversion ratio is very high [102].

Unlike conduction and switching losses, which are inevitable and can only be reduced up to some extent, synchronization losses are avoidable and can be almost completely eliminated. If the dead time and the duration of  $M_P$  ON time are adaptive and accurate for all possible input voltages, synchronization losses might be suppressed to almost negligible levels compared to conduction or switching losses. The low power control of the boost converter is responsible for this task, as it will be presented in more detail in the next chapter.

### 4.3 Impact of Losses on Efficiency

In the previous sections, the losses within the boost converter have been identified and analyzed. As it has been demonstrated, the synchronization losses,  $P_{sync}$ , can be almost entirely eliminated by the adequate timings of the driving signals generated in the control circuitry. Implementation of such control will be covered in the next chapter as well as the techniques to minimize the power consumption of the control. On the other hand, the conduction and switching losses,  $P_{cond}$  and  $P_{sw}$  respectively, are inevitable and can only be reduced up to some extent. In most converters, these losses are the main contributors to the sum  $(P_{loss} + P_{control})$ , which defines the efficiency given by Eq. (4.13), and they have to be minimized in order to achieve high efficiency.

The total losses within the converter can be expressed as [35, 97, 99]:

$$P_{loss} = P_{cond} + P_{sw} + P_{sync}. \quad (4.41)$$

Assuming that the synchronization losses are eliminated by the control, the total losses can be approximated as:

$$P_{loss} = \underbrace{P_{cond,N} + P_{cond,P} + P_{cond,L}}_{\text{conduction losses}} + \underbrace{P_{sw,N} + P_{sw,P} + P_{sw,X}}_{\text{switching losses}}, \quad (4.42)$$

where  $P_{cond,N}$ ,  $P_{cond,P}$ ,  $P_{cond,L}$ ,  $P_{sw,N}$ ,  $P_{sw,P}$  and  $P_{sw,X}$  are given by Eq. (4.18), (4.19), (4.20), (4.24), (4.25) and (4.26) respectively. The terms in Eq. (4.42) can be rearranged according to the impact of the individual components as:

$$P_{loss} = \underbrace{P_{cond,N} + P_{sw,N}}_{\text{nFET}} + \underbrace{P_{cond,P} + P_{sw,P}}_{\text{pFET}} + \underbrace{P_{cond,L}}_{\text{inductor}} + \underbrace{P_{sw,X}}_{\text{node X}}. \quad (4.43)$$

The losses related directly to  $M_N$  can be determined with Eq. (4.18) and (4.24):

$$P_{cond,N} + P_{sw,N} = \frac{I_{L,max}^2}{3} R_N \tau_N f_s + C_N V_{out}^2 f_s. \quad (4.44)$$

If  $\tau_N$  is replaced with  $\tau_N = DT_s = \frac{D}{f_s}$ , similar as in Eq. (4.9), the Eq. (4.44) becomes:

$$P_{cond,N} + P_{sw,N} = \frac{V_{in}^2 D^3}{3L^2 f_s^2} R_N + C_N V_{out}^2 f_s. \quad (4.45)$$

By observing the Eq. (4.45), several conclusions can be drawn. The losses related to  $M_N$  can be reduced by increasing the inductance of the inductor. However, the inductor's physical size and, consequently, its inductance are limited by the application, so there is a small room for reducing the losses in this way. The duty ratio of the converter and its switching frequency are fixed by the maximum power extraction (input matching), as it will be seen in the next section. Therefore, only the ON resistance of the switch and its gate capacitance are left for manipulation. The Eq. (4.45) can be also expressed as:

$$P_{cond,N} + P_{sw,N} = \frac{V_{in}^2 D^3}{3L^2 f_s^2} \frac{R'_N}{W_N} + C'_N W_N V_{out}^2 f_s, \quad (4.46)$$

where  $R'_N$  is the ON resistance of  $M_N$  per unit width,  $C'_N$  is the capacitance of  $M_N$  per unit width and  $W_N$  is the width of the transistor  $M_N$ . Therefore, as the transistor size is increasing the switching losses are also increasing while the conduction losses are decreasing. This means that there is an optimal transistor size for which the losses are minimized, and it is reached when [35, 97]:

$$\frac{\partial P_{loss}}{\partial W_N} = 0. \quad (4.47)$$

The losses related to nFET, as well as the losses related to the node X, depend on  $W_N$ , while other terms in Eq. (4.43) are independent of  $W_N$  and can be ignored (their derivative with respect to  $W_N$  is zero). Therefore, it can be written:

$$\frac{\partial P_{loss}}{\partial W_N} = \frac{\partial (P_{cond,N} + P_{sw,N} + P_{sw,X})}{\partial W_N} = 0, \quad (4.48)$$

which can be simplified as:

$$\frac{\partial (k_1 \frac{1}{W_N} + k_2 W_N)}{\partial W_N} = 0, \quad (4.49)$$

where  $k_1 = \frac{V_{in}^2 D^3}{3L^2 f_s^2} R'_N$  and  $k_2 = (C'_N + \frac{1}{2} C'_{jN} + \frac{1}{2} C'_{ovN}) V_{out}^2 f_s$ . Finally, the optimal width of  $M_N$ ,  $W_{N,opt}$ , can be derived as:

$$W_{N,opt} = \sqrt{\frac{k_1}{k_2}} = \sqrt{\frac{V_{in}^2 D^3 R'_N}{3V_{out}^2 L^2 f_s^3 (C'_N + \frac{1}{2} C'_{jN} + \frac{1}{2} C'_{ovN})}}. \quad (4.50)$$

Similarly, the optimal width of  $M_P$ ,  $W_{P,opt}$ , can also be derived as:

$$W_{P,opt} = \sqrt{\frac{V_{in}^3 D^3 R'_P}{3V_{out}^3 L^2 f_s^3 (C'_P + \frac{1}{2}C'_{jP} + \frac{1}{2}C'_{ovP})}}. \quad (4.51)$$

It is interesting to notice that the optimal transistor's ratio, derived from Eq. (4.50) and (4.51), depends only on the input and output voltages and the used technology as:

$$\frac{W_{N,opt}}{W_{P,opt}} \approx \sqrt{\frac{V_{out}\mu_P}{V_{in}\mu_N}}, \quad (4.52)$$

where  $\mu_N$  and  $\mu_P$  are the charge-carrier mobilities of  $M_N$  and  $M_P$ , respectively.

It can be seen from the expressions (4.50), (4.51) and (4.52) that the optimal switch sizes depend on the input voltage. Therefore, the operation of the converter is optimal for a particular value of the input voltage and as  $V_{in}$  moves away from the optimal point, the conduction and switching losses sum is no longer minimized. However, this sizing procedure is still an effective way to keep the losses under control. The input voltage according to which the switches are sized should be located in the middle of a full range, or it should be a value which occurs most often.

The inductor value is also critical for the efficient operation of a boost converter. In fact, a higher inductor value reduces the conduction losses, as it can be seen in Eq. (4.18). On the other hand, a higher inductance either requires a larger physical size of an inductor, which is quite limited in implantable applications, or introduces a higher parasitic series resistance, which actually increases the conduction losses. An inductor of 10  $\mu\text{H}$  is used in this work as a good trade-off between the losses, parasitic resistance and form factor.

#### 4.4 Maximum Power Extraction

The thermoelectric energy harvester can be modeled as a voltage source in series with a resistor, as described in Eq. (3.7) and (3.8). To extract the maximum possible power from such source, an adequate resistance has to be presented to the harvester. According to Fig. 4.9, if the resistance seen at the input of the converter is  $R_{in}$ , the power extracted by the converter is given by:

$$P_{in} = \frac{V_{in}^2}{R_{in}} = \frac{(V_T \frac{R_{in}}{R_{in}+R_T})^2}{R_{in}} = V_T^2 \frac{R_{in}}{(R_{in} + R_T)^2}. \quad (4.53)$$

This power is maximum for:

$$\frac{\partial P_{in}}{\partial R_{in}} = 0, \quad (4.54)$$

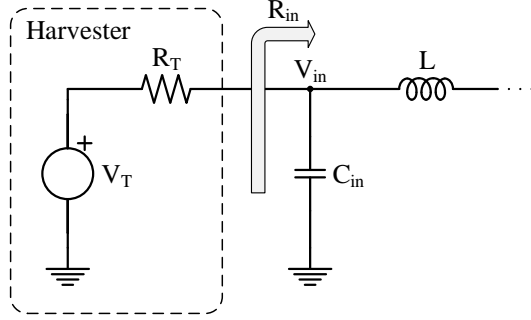


Figure 4.9: Simple input matching.

which is obtained for  $R_{in} = R_T$ . On the other hand, the input resistance of the boost converter is given by [38, 69]:

$$R_{in} = \frac{V_{in}}{\overline{I_{in}}}, \quad (4.55)$$

where  $\overline{I_{in}}$  is the average input current of the converter. This current can be expressed as [38, 69]:

$$\overline{I_{in}} = \frac{I_{L,max}}{2} \frac{\tau_N + \tau_P}{T_s} = \frac{V_{in} \tau_N (\tau_N + \tau_P)}{2LT_s}. \quad (4.56)$$

By introducing Eq. (4.56) in (4.55),  $R_{in}$  becomes:

$$R_{in} = \frac{2LT_s}{\tau_N (\tau_N + \tau_P)}. \quad (4.57)$$

Assuming that  $V_{in} \ll V_{out}$  implies  $\tau_P \ll \tau_N$ , so Eq. (4.57) can be approximated as:

$$R_{in} \approx \frac{2Lf_s}{D^2}. \quad (4.58)$$

Therefore, to extract the maximum possible power from the harvester, in this case from the thermoelectric energy harvester, the switching frequency,  $f_s$ , and the duty cycle of the boost converter,  $D$ , have to be fixed [38, 69, 95, 97]. Consequently, the internal resistance of the harvester and the input resistance of the converter are constantly matched, and no maximum power point tracking (MPPT) algorithms are needed. The control circuitry is responsible for keeping the resistances matched, by fixing the terms in Eq. (4.58).

## 4.5 Start-up Circuitry

The start-up circuitry is one of the major challenges in the PMU implementation. The input voltage of the PMU is much lower than the voltage necessary to successfully operate the switches, and the storage capacitor has to be pre-charged to the adequate level through another path. Usually, an additional block is responsible for successful start-up, bypassing the input converter, as it is shown in Fig. 4.1.

A few solutions for implementing such block can be found in the literature [69,95,96,103]. In [96], a bulky transformer is utilized to self-start-up the converter. The secondary coil of the transformer is used to grow the oscillations which are then used to start-up the boost converter. The start-up circuit is completely electrical and starts from only 40 mV, but it requires an external transformer with area and cost penalty. In [69], a mechanical switch implemented with MEMS is used for the start-up. Since the mechanical switch changes its state only once during the start-up, to build up enough energy a large inductor of 22  $\mu$ H is also required. The achieved start-up voltage of 35 mV is the lowest one reported. One recent work [95] uses another external inductor to build up oscillations and start up the auxiliary boost converter. The oscillator is a simple voltage-limited LC-tank, followed by the voltage multiplier to boost the amplitude. Another boost converter is used later for high efficient conversion. This approach employs three external inductors and starts-up from 50 mV. In [103], a self-start-up technique, which uses a ring oscillator and a low efficiency charge pump to start from the input voltage of 95 mV, is presented. This method requires the post-fabrication trimming of the voltage threshold, which increases the cost.

Another viable solution is a start-up through RF harvesting with a dedicated RF source, such as one implemented in [26]. This solution is convenient because the antenna used for communication purposes can be used for the start-up [104]. The efficiency of the energy transfer does not have to be high since it is a one-time process.

## 4.6 Summary

The input converter is the critical block of the PMU. The architecture of the input converter is proposed taking into consideration its main requirements, namely its size and voltage conversion efficiency. Since the efficiency of the converter is defined by its losses, a detailed analysis of all potential sources of losses is conducted. In addition, their impact on the overall efficiency is estimated. The sources of inevitable losses, such as conduction and switching losses, are identified, and the input converter design procedure for minimizing these losses is proposed. At the same time, avoidable synchronization losses related to the proper timings are also addressed in detail. However, their suppression depends on the control circuit that will be tackled in the next chapter. Finally, the maximum power extraction strategy and the potential solutions for the start-up circuits are presented.

## Chapter 5

# Low Power Control

The control circuit is responsible for the proper functionality of the boost converter, which is defined by the switching diagram shown in Fig. 4.3 and the steady state condition given by Eq. (4.7). Besides that, the control circuit ensures that synchronization losses are minimized so that the conversion efficiency of the converter, given by Eq. (4.13), is as high as possible. Therefore, as explained in the previous chapter, the switching timings have to be well defined and adjustable at the same time. Finally, the power consumption of the control circuit is also reducing the overall efficiency and, because of that, it is limited to very low levels. To summarize, the control has to accomplish accurate and adaptive switching under the extreme power limitations.

The implementation of an efficient control for a boost converter targeting implantable thermoelectric energy harvesting applications is the main focus of this chapter. First, the architecture of the proposed control will be presented. Second, the signal generator for driving the nFET switch will be implemented to obtain MPE defined in the section 4.4. Third, Zero-Current Switching (ZCS) and Zero-Voltage Switching (ZVS) techniques for driving the pFET switch will be proposed and implemented to suppress synchronization losses described in the section 4.2.3. Finally, the simulation results will be presented and discussed.

### 5.1 Proposed Control Architecture

As it was already mentioned, the control has to fulfill several tasks related to accurate switching while consuming a very low power. This means that it has to be relatively simple but highly effective at the same time. The control in [35] is based on a simple idea, which can be described as following: i) After the transistor  $M_P$  turns off, by observing the voltage  $V_X$ , the information whether the transistor  $M_P$  is turned off early ( $V_X$  is high) or late ( $V_X$  is low) can be obtained, as explained in the section 4.2.3 and illustrated in Fig. 4.6. ii) The voltage  $V_X$  can be sensed by using a simple D flip-flop to map this information into a digital bit,  $b_0$ . ii)

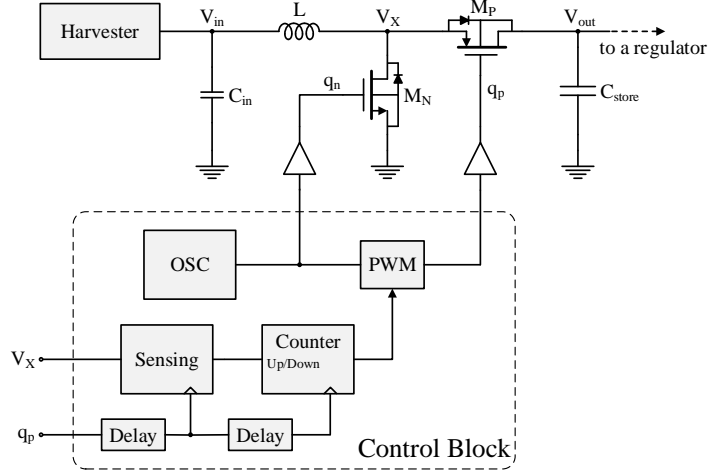


Figure 5.1: Block diagram of the traditional control circuit.

By adjusting the duration of the  $M_N$  ON time ( $\tau_N$ ), according to the value of  $b_0$ , the turn-off timing of  $M_P$  gets closer to the accurate value after every switching cycle. Following this idea, a fully digital control, which does not consume any static power and roughly achieves ZCS, can be implemented. However, since  $\tau_N$  is altered, the input resistance of the boost converter, given by Eq. (4.55), is also changed. As a result, the converter is not extracting the maximum possible power from the energy harvester, as explained in the section 4.4. This issue is recognized and solved in [69], where instead of  $\tau_N$ , the duration of the  $M_P$  ON time ( $\tau_P$ ) is adjusted. Similar control is used in most of related work [35, 69, 95, 97]. The simplified block diagram of such control is shown in Fig. 5.1. An oscillator generates the fixed frequency and duty ratio signal ( $q_n$ ), which drives  $M_N$  for MPE. A 1-bit information  $b_0$ , obtained from sensing the voltage  $V_X$ , controls the counter value up ( $b_0 = 1$ ) or down ( $b_0 = 0$ ). The counter value then adjusts the duration of  $\tau_P$  through Pulse-Width-Modulation (PWM) block, accordingly. As a result, MPE and relatively accurate ZCS are achieved. However, even in the improved version of the control, presented in [69], several issues can be identified. Since the counter value is continuously adjusted, the nominal value of  $\tau_P$  is never reached. The transistor  $M_P$  will always switch around the nominal point, slightly early or slightly late. Moreover, losses related to  $M_P$  turn-on timing, i. e. dead time losses, are not addressed at all. Therefore, the existing solution can be improved by eliminating dead time losses and further reducing the losses related to  $M_P$  turn-off timing.

The proposed control, which targets to improve the existing solution, is shown in Fig. 5.2 [105]. Unlike in the traditional solution, the voltage  $V_X$  is sensed two



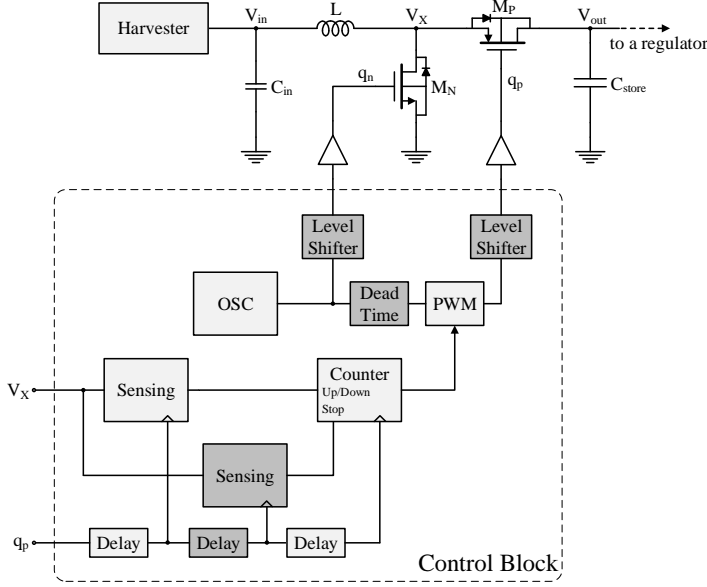


Figure 5.2: Block diagram of the proposed control circuit.

times to obtain the 2-bit information, which stops the counter when the nominal duration of  $\tau_P$  is reached. Moreover, an additional block is added to achieve ZVS and to eliminate the dead time losses. More details about these improvements will be provided in the following sections. In addition, the power consumption of the control circuit is minimized by following the techniques presented in [106]. Particularly, the power supply voltage of the control is reduced to 1 V, the short circuit currents of logic gates are limited by making their input and output edges equal, and subthreshold leakage is minimized by reducing  $\frac{W}{L}$  of transistors in the logic gates.

Since the power supply voltage of the control is reduced to 1 V, the level shifters are introduced to adapt the voltage level of digital signals to the voltage level of the output. This is necessary in order to drive the switches correctly [107]. The conventional level shifter circuit is used, as it is shown in Fig. 5.3. The switch drivers are implemented as tapered buffers of  $n$  stages, with a scaling factor  $f_{scale}$ , where  $n$  and  $f_{scale}$  are given by [108]:

$$n = \ln \left( \frac{C_g}{C_{g,min}} \right), \quad (5.1)$$

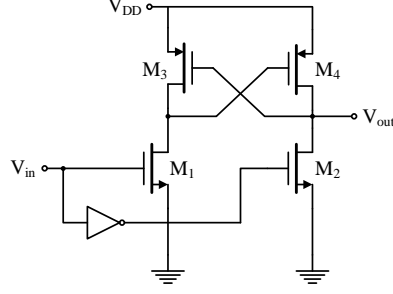


Figure 5.3: Level shifter schematic.

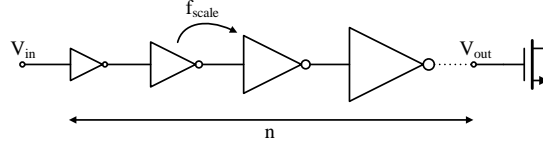


Figure 5.4: Switch driver schematic.

$$f_{scale} = \sqrt[n]{\frac{C_g}{C_{g,min}}}, \quad (5.2)$$

where  $C_g$  is the gate capacitance of the driven switch and  $C_{g,min}$  is the gate capacitance of the minimal sized inverter. The circuit of these drivers is shown in Fig. 5.4.

## 5.2 Driving the nFET Switch

The maximum power extraction (MPE) is obtained when the input resistor of a boost converter is matched to the internal resistance of an energy harvester, as it is explained in the section 4.4. The input resistance of a boost converter is given by Eq. (4.58). On the other hand, the internal resistance of a thermoelectric energy harvester depends on the used device. For instance, the internal resistance of the device presented in [72] is only  $5 \Omega$ , while the internal resistance of [73] is  $300 \Omega$ . In this work, an intermediate value of  $100 \Omega$  is adopted. Considering Eq. (4.58),

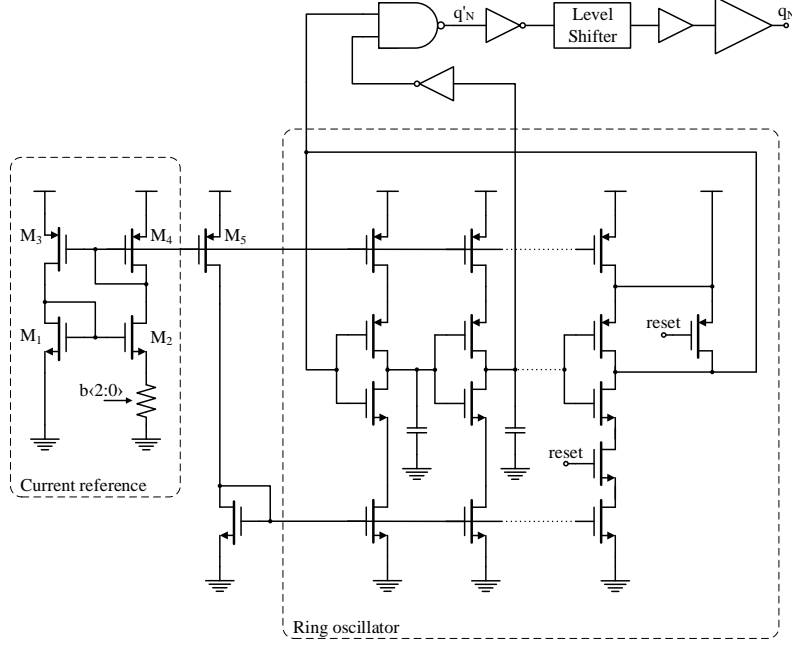


Figure 5.5: nFET switch signal generator [105].

the switching frequency,  $f_s$ , can be calculated as:

$$f_s \approx \frac{R_{in} D^2}{2L}. \quad (5.3)$$

Assuming the inductor of  $10 \mu\text{H}$ , adopted in the section 4.3, and 50% duty cycle, which is often used because of its simple implementation [35, 69, 95], the corresponding operating frequency should be equal to 1.25 MHz. However, such high operating frequency introduces high switching losses and increases the power consumption of the control circuit. For this reason, the duty cycle and, consequently, the operating frequency are scaled down to 10% and 50 kHz, respectively. These values provide an appropriate trade-off between conduction losses, switching losses, implementation complexity and the power consumption of the control circuit.

The control signal generator for driving the transistor  $M_N$  with the fixed switching frequency and duty cycle is shown in Fig. 5.5 [105]. Note that the duration of  $M_N$  ON time, given by  $\tau_N = \frac{D}{f_s}$ , is also fixed. A current reference provides biasing currents for an ultra-low power ring oscillator. The oscillator generates two 50% duty cycle clock signals, which are combined in logic gates to obtain a 10% duty cycle signal for driving  $M_N$ .

The current reference is operating in the weak inversion region. The relation between the gate-source voltages of the transistors  $M1$  and  $M2$  can be written as:

$$V_{GS1} = V_{GS2} + I_{D2}R_s, \quad (5.4)$$

where  $I_{D2}$  is the drain current of  $M2$ . For  $V_{DS} > 0.1$  V,  $V_{GS}$  of the transistor, which is operating in weak inversion, can be approximated as [109]:

$$V_{GS} = V_{TH} + nV_T \ln \left( \frac{I_D}{2n\beta V_T^2} \right), \quad (5.5)$$

where  $V_{TH}$  is the threshold voltage,  $n$  is the subthreshold slope factor,  $V_T (= kT/q)$  is the thermal voltage,  $k$  is the Boltzmann constant,  $T$  is the absolute temperature,  $q$  is the elementary charge,  $\beta (= \mu C_{ox} \frac{W}{L})$  is the gain factor,  $\mu$  is the carrier mobility and  $C_{ox}$  is the gate-oxide capacitance. The current mirror consisting of transistors  $M3$ ,  $M4$  and  $M5$  assures that  $I_{bias} = I_{D1} = I_{D2}$ . Combining Eq. (5.4) and (5.5), the biasing current can be expressed as:

$$I_{bias} = \frac{nV_T \ln \left( \frac{\beta_2}{\beta_1} \right)}{R_s}. \quad (5.6)$$

The resistance  $R_s$  and the transistors  $M1$  and  $M2$  are sized in such way so that the obtained biasing current is equal to 30 nA.

The current starved ring oscillator consists of ten inverter stages and one nand stage for resetting/disabling purposes. Its operating frequency is approximated as [110]:

$$f_s \approx \frac{1}{2Nt_d} = \frac{I_{bias}}{NV_{DD}C_L}, \quad (5.7)$$

where  $N$  is the number of delay stages, which, in this case, is equal to ten because the nand stage is not loaded. The operating frequency of 50 kHz is obtained by proper sizing the loading capacitors. The delay between two extracted clock signals corresponds to two inverter stages and is equal to  $1/(10f_s)$ , so the resulting signal ( $q_N$ ) has a duty cycle of 10%. A 3-bit signal  $b(2:0)$  controls the resistance  $R_s$  and, consequently, the biasing currents to adjust the operating frequency for process variations, if necessary.

### 5.3 Zero-Current Switching

Since the  $M_N$  ON time duration ( $\tau_N$ ) is fixed by the input matching, the duration of  $M_P$  ON time ( $\tau_P$ ) has to be adjusted in order to meet the condition (4.34) and achieve efficient ZCS. In [35], a simple method is proposed to obtain ZCS, as explained in the section 5.1. However, as a result, the transistor  $M_P$  will always turn-off either slightly early or slightly late. As it is shown in Eq. (4.27) and

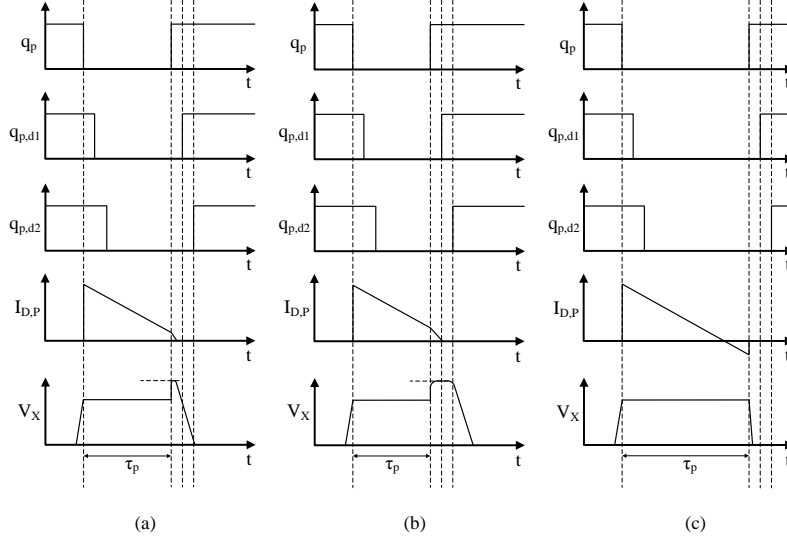


Figure 5.6: Waveforms of a pFET switch turning off (a) slightly early, (b) early and (c) late [105].

(4.28), it is much more efficient to turn-off  $M_P$  slightly early than late. This fact is exploited in this work to improve the ZCS method proposed in [35], which is also used in other related work [69, 95, 97].

In the method proposed in this work, the voltage  $V_X$  is sensed two times after the  $M_P$  is turned-off. The sensing timings are delayed with respect to each other for a fixed duration, as it is illustrated in Fig. 5.6. The 2-bit digital signal ( $b_1b_0$ ) provides the information whether  $M_P$  is turned-off late ( $b_1b_0 = 00$ ), early ( $b_1b_0 = 11$ ) or on-time ( $b_1b_0 = 10$ ). The reading  $b_1b_0 = 01$  is not expected to occur. The counter value, and, consequently,  $\tau_P$ , is updated according to  $b_1b_0$ , as it is illustrated in Table 5.1. As a result, when  $\tau_P$  reaches nominal duration, the counter is stopped,

Table 5.1: Adjusting the counter value according to the sensed signal.

| $b_1b_0$ | Counter Action |
|----------|----------------|
| 00       | down           |
| 01       | —              |
| 10       | stop           |
| 11       | up             |

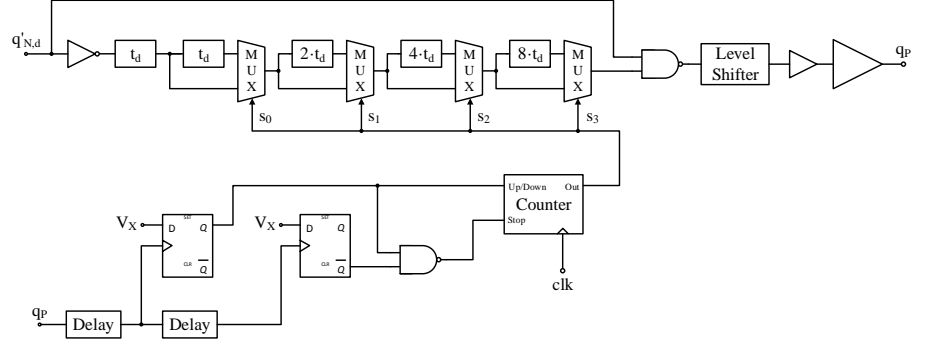


Figure 5.7: pFET switch signal generator [105].

and the boost converter continues switching at the nominal point achieving ZCS, continuously.

The implementation of the proposed method is shown in Fig. 5.7 [105]. The sensing of the voltage  $V_X$  is triggered by the delayed rising edge of the signal  $q_P$ , which is driving the transistor  $M_P$ . Based on the counter value, the PWM block adjusts the duration of  $\tau_P$  for the next switching cycle. The PWM is implemented as one-shot signal generator with controllable signal width. The one-shot pulse is triggered by the rising edge of signal  $q'_{N,d}$ , which is the delayed version of the signal  $q'_N$  from the Fig. 5.5. The 4-bit counter is used in this work as a good trade-off between the accuracy of  $\tau_P$  and complexity. It is important to note that the counter is modified so it does not reset back to zero when the highest value is stored and signal *up* is active, but it rather keeps the highest value locked. Similarly, when zero is stored and signal *down* is active, the counter stays at zero.

Delay blocks are implemented as a simple digital delay elements consisting of two inverters and a loading capacitor between them. The D flip-flops are transmission-gate flip-flops with internal gate isolation (TGFF), which are proven to be energy efficient [111].

## 5.4 Zero-Voltage Switching

As it was concluded in the section 4.2.3, the dead time has to be adaptive to suppress the synchronization losses related to  $M_P$  turn-on timing. The duration of the dead time for which these losses are eliminated relates to the duration of  $\tau_P$ , as it can be seen in Eq. (4.35). On the other hand, the value stored in the counter corresponds to the duration of  $\tau_P$ . Therefore, the same counter can be used to control the adaptive dead time. However, the counter value is proportional to  $\tau_P$ , while the dead time relates to  $\tau_P$  as  $\propto \frac{1}{\tau_P}$ . For this reason, the nonlinear decoding

Table 5.2:  $\tau_P$ , decoder outputs and dead time corresponding to counter values.

| $s_3 s_2 s_1 s_0$ | $\tau_P$ [ns] | $d_6 d_5 d_4 d_3 d_2 d_1 d_0$ | $t_{dead}$ [ps] |
|-------------------|---------------|-------------------------------|-----------------|
| 0000              | 20            | 0000000                       | 2500            |
| 0001              | 32            | 0000001                       | 1600            |
| 0010              | 44            | 0000010                       | 1200            |
| 0011              | 56            | 0000100                       | 900             |
| 0100              | 68            | 0001000                       | 800             |
| 0101              | 80            | 0001000                       | 800             |
| 0110              | 92            | 0010000                       | 600             |
| 0111              | 104           | 0010000                       | 600             |
| 1000              | 116           | 0100000                       | 500             |
| 1001              | 128           | 0100000                       | 500             |
| 1010              | 140           | 0100000                       | 500             |
| 1011              | 152           | 0100000                       | 500             |
| 1100              | 164           | 1000000                       | 300             |
| 1101              | 176           | 1000000                       | 300             |
| 1110              | 188           | 1000000                       | 300             |
| 1111              | 200           | 1000000                       | 300             |

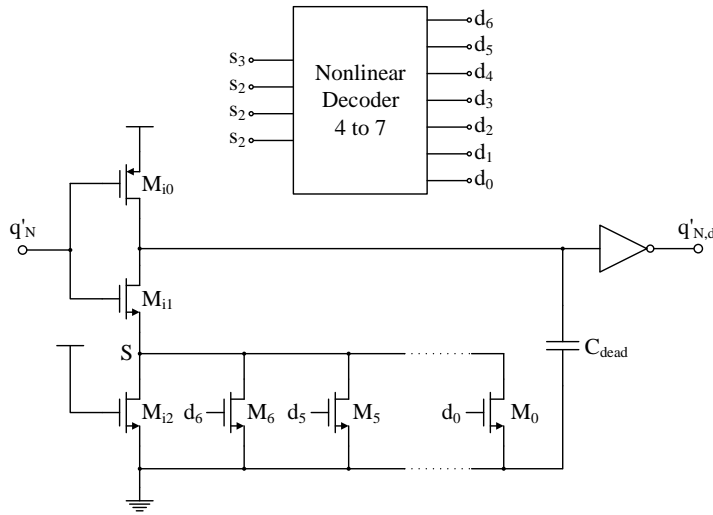


Figure 5.8: Adaptive dead time circuit [102].

of the counter value has to be done before generating the dead time. Table 5.2 presents the durations of  $\tau_P$ , the decoder outputs and the dead time durations corresponding to the actual counter values. Since the 4-bit counter is used in this work, sixteen different durations of the dead time can be implemented. However, usually good approximations are obtained with lower number of different durations, such as eight in this case. This is because the accurate dead time values are getting closer to each other as the counter value is increasing. The value of capacitance  $C_X$  is assumed to be equal to 5 pF.

The implementations of the adaptive dead time circuit are shown in Fig. 5.8 [102, 105]. The adaptive dead time circuit is acting as a digitally programmable delay element. It delays the rising edge of the signal  $q'_N$  and creates the signal  $q'_{N,d}$ , which afterwards triggers the one-shot signal generator (PWM) from the Fig. 5.7.

## 5.5 Simulation Results

The proposed control is applied to the boost converter presented in the section 4.1, as it is illustrated in Fig. 5.2. The parameters of the boost converter are summarized in Table 5.3. Transistors are sized according to Eq. (4.50) and (4.51) to minimize the losses, as it is explained in the section 4.3. The input voltage is varied between 20 mV and 200 mV, while the output voltage is fixed to around 2 V. The efficiency of the converter is compared to the state-of-the-art converter [35] for different conversion ratios, as it is shown in Fig. 5.9. The converter and the control proposed in this work maintain high efficiency for much higher voltage conversion ratios. This is mainly due to a very low power consumption of the corresponding control circuitry. In addition, efficiencies of the same control circuit,

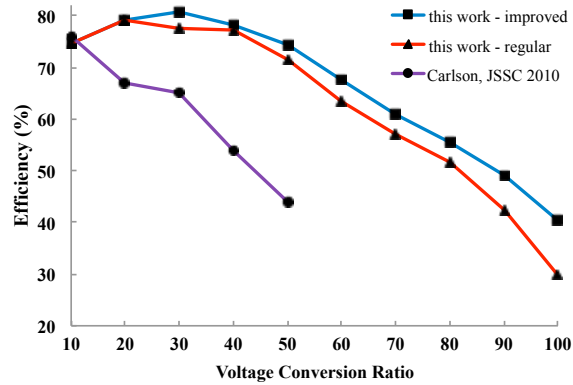
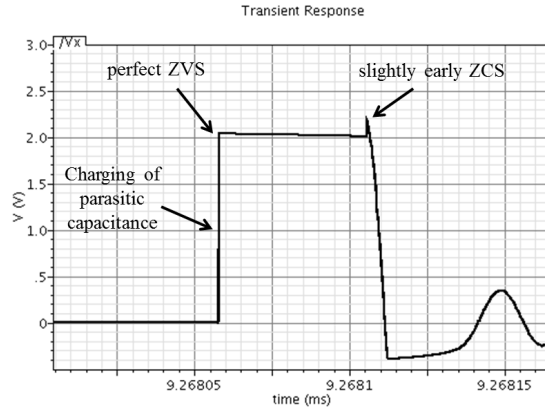


Figure 5.9: Efficiency comparison between [35] and this work. Image from [105].



Table 5.3: Parameters of the proposed boost converter.

| $W_N$              | $W_P$             | $L$              | $R_L$        | $C_{in}$        | $C_{store}$ |
|--------------------|-------------------|------------------|--------------|-----------------|-------------|
| 1800 $\mu\text{m}$ | 600 $\mu\text{m}$ | 10 $\mu\text{H}$ | 0.5 $\Omega$ | 1 $\mu\text{F}$ | 30 nF       |

Figure 5.10: Waveform of the voltage  $V_X$  [105].

before and after introducing the improvements in ZCS technique and additional dead time block (ZVS), are presented. Efficiency enhancement, when the proposed techniques are used, is evident and can reach up to 10% at high voltage conversion ratios.

The simulation results, presented in Fig. 5.10, show that ZCS and ZVS are successfully achieved. The accurate dead time duration, which corresponds to Fig. 4.7(a), is obtained, as well as slightly short  $\tau_P$ , which corresponds to Fig. 5.6(a). At the same time, the power consumption of the complete control circuit is only 620 nW.

The simulated efficiency improvement, shown in Fig. 5.11, was obtained by adding the dead time block and it corresponds to the values estimated in Eq. (4.40). This proves the accuracy of the derived expressions and effectiveness of the proposed adaptive dead time circuit. The power consumption of the adaptive dead time circuit is only 10 nW, and it provides the maximum efficiency improvement of 2.2%.

## 5.6 Summary

The control circuit determines the functionality and the efficiency of the boost converter. The ultra low power control, which employs MPE, ZCS and ZVS, is

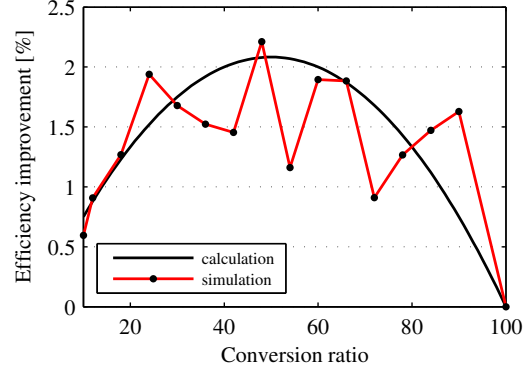


Figure 5.11: Efficiency improvement due to the adaptive dead time [102].

proposed and combined with previously presented boost converter to achieve efficient energy transfer from a thermoelectric harvester to biosensor circuits.

The comparison of the boost converter driven by the proposed control with the related work is shown in Table 5.4. This work demonstrates superior voltage conversion efficiency, especially when it is compared to the work with higher output voltages (conversion ratio) [69, 96]. Therefore, it shows a good potential for implementing an efficient, high conversion ratio PMU, which is required for enabling autonomous implantable biosensors. It should be noted that the control circuit is powered from an ideal 1 V source and the results are obtained from simulations. Therefore, when this supply voltage is generated from the output capacitor, some additional power will be lost.

Table 5.4: Comparison of the proposed boost converter with state-of-the-art work.

|                            | <b>Carlson<br/>[35]</b> | <b>Ramadas<br/>[69]</b> | <b>Im<br/>[96]</b>  | <b>Weng<br/>[95]</b> | <b>Chen<br/>[39]</b> | <b>This<br/>Work</b> |
|----------------------------|-------------------------|-------------------------|---------------------|----------------------|----------------------|----------------------|
| <b>Year</b>                | 2010                    | 2011                    | 2012                | 2013                 | 2015                 | 2015                 |
| <b>Process</b>             | 0.13- $\mu\text{m}$     | 0.35- $\mu\text{m}$     | 0.13- $\mu\text{m}$ | 65-nm                | 0.18- $\mu\text{m}$  | 0.18- $\mu\text{m}$  |
| <b>Output<br/>Voltage</b>  | 1 V                     | 1.8 V                   | 2.0 V               | 1.2 V                | 0.5 V                | 2.0 V                |
| <b>Peak<br/>Efficiency</b> | 75 %                    | 58 %                    | 61 %                | 73 %                 | 83.4 %               | 81 %                 |

## Chapter 6

# Conclusion and Future Work

The available energy harvesting sources in the human body are investigated, the biosensor's powering requirements are identified and the potential interface circuits are explored. Additionally, an efficient PMU for thermoelectric energy harvesting is proposed for self-powered implantable biosensors. The proposed PMU consists of a customized boost converter and an efficient control circuit. It acts as an interface between a thermoelectric energy harvester and circuits of an implantable biosensor. The boost converter is designed so that the sum of conduction and switching losses is minimized. In addition, synchronization losses are successfully identified, estimated and eliminated by the ultra-low power control circuit. As a result, the proposed PMU achieves 81% efficiency and enables self-powered implantable biosensors. When compared to the state-of-the-art work, the PMU demonstrates higher efficiencies at voltage conversion ratios above 20.

Even if the synchronization losses are completely eliminated and the power consumption of the control is further reduced, it is unlikely that the efficiency of the proposed PMU can exceed 90%. This is because the conduction and switching losses are inevitable, and their minimized sum still reduces the efficiency in standard CMOS processes with at least 10%. An advanced process technology, with lower ON resistances of the transistors and lower parasitic capacitances, may enable efficiencies higher than 90%.

Although the work in this thesis fulfills the main objectives defined in the section 1.3, several shortcomings and potential improvements are identified for the future work:

- In the section 4.3, while calculating the optimal width of switches to minimize the impact of inevitable losses, the leakage of the switching transistors is neglected. However, the subthreshold leakage of switches may become significant at very low power levels, since it is not scaling with the input power. In addition, the subthreshold leakage is proportional to the transistor width, and, therefore, it should be included in the optimal width calculations.

- It is mentioned in the section 5.1 that the voltage supply of the control circuit is reduced to 1 V. However, this voltage supply is not generated in this work, but instead an ideal voltage source is used. In reality, it has to be obtained from the output voltage either by using another converter (step-down) or by adding a second output to the boost converter.
- Some less critical, but still important, blocks of the PMU are not implemented in this work including a start-up circuit, a storage monitor, a bandgap, and an output regulator. These blocks will be implemented in the future work to obtain the complete PMU solution, as it is presented in Fig. 4.1.
- State-of-the-art thermoelectric energy harvesters provide up to  $100 \mu\text{W}/\text{cm}^2$  at low temperature differences, such as within the human body. Considering the size limitation of implantable devices, the expected output power is around 20 to  $30 \mu\text{W}$  in the best case. Assuming 80% efficiency of the PMU, the power provided to the biosensor circuit can be less than  $20 \mu\text{W}$ . While this amount of power is sufficient for some biosensors [26], it can not support all possible applications. The average power consumption of a biosensor has to be lower than the provided amount. Otherwise, another energy harvesting source can be added to obtain higher power and improved reliability, at the price of the system size and complexity. In such cases, a multi-source PMU has to be considered.

# Bibliography

- [1] I. Akyildiz, W. Su, Y. Sankarasubramaniam, and E. Cayirci, “Wireless sensor networks: a survey,” *Comput. Netw.*, vol. 38, pp. 393–422, 2002.
- [2] J. Yick, B. Mukherjee, and D. Ghosal, “Wireless sensor network survey,” *Comput. Netw.*, vol. 52, pp. 2292–2330, 2008.
- [3] Z. Nauman, S. Iqbal, M. I. Khan, and M. Tahir, “WSN-based fire detection and escape system with multi-modal feedback,” in *Multimedia Communications, Services and Security*, 2011, pp. 251–260.
- [4] S. Kim, S. Pakzad, D. Culler, J. Demmel, G. Fenves, S. Glaser, and M. Turon, “Health Monitoring of Civil Infrastructures Using Wireless Sensor Networks,” in *Proc. 6th International Symposium on Information Processing in Sensor Networks*, 2007, pp. 254–263.
- [5] S. I. Association, “International Technology Roadmap for Semiconductors, Radio Frequency and Analog/Mixed-Signal Technologies Summary,” Tech. Rep., 2013. [Online]. Available: <http://www.itrs.net/reports.html>
- [6] B. Bhushan, “MEMS/NEMS and BioMEMS/NEMS: Materials, Devices, and Biomimetics,” in *Nanotribology and Nanomechanics: Nanotribology, Biomimetics and Industrial Applications, Vol 2*, 2011, pp. 833–945.
- [7] C. Marli and C. a. Paiva, “Biosensors for Health Applications,” in *Biosensors for Health, Environment and Biosecurity*, 2011, pp. 71–86.
- [8] S. Vaddiraju, I. Tomazos, D. Burgess, F. Jain, and F. Papadimitrakopoulos, “Emerging Synergy between Nanotechnology and Implantable Biosensors: A Review,” *Biosens. Bioelectron.*, vol. 25, no. 7, pp. 1553–1565, 2010.
- [9] J. S. Perlmutter and J. W. Mink, “Deep brain stimulation,” *Annu. Rev. Neurosci.*, vol. 29, pp. 229–257, 2006.
- [10] W. Greatbatch and C. F. Holmes, “History of implantable devices,” *IEEE Eng. Med. Biol. Mag.*, vol. 10, no. 3, pp. 38–41, 1991.

- [11] “By Professor Marko Turina, University Hospital, Zurich [CC BY 3.0 (<http://creativecommons.org/licenses/by/3.0>)], via Wikimedia Commons.” [Online]. Available: [http://commons.wikimedia.org/wiki/File/%3AFirst\\\_pacemaker\\\_ \(Siemens-Elerna\\\_1958\).jpg](http://commons.wikimedia.org/wiki/File/%3AFirst\_pacemaker\_ (Siemens-Elerna\_1958).jpg)
- [12] M. R. Yuce, “Implementation of wireless body area networks for healthcare systems,” *Sens. Actuators A*, vol. 162, no. 1, pp. 116–129, Jul. 2010.
- [13] “By Intel Free Press [CC BY-SA 2.0 (<http://creativecommons.org/licenses/by-sa/2.0>)], via Wikimedia Commons.” [Online]. Available: [http://commons.wikimedia.org/wiki/File/%3ACardioMEMS\\\_wireless\\\_sensor\\\_with\\\_quarter.png](http://commons.wikimedia.org/wiki/File/%3ACardioMEMS\_wireless\_sensor\_with\_quarter.png)
- [14] S. A. P. Haddad, R. P. M. Houben, and W. A. Serdijn, “The evolution of pacemakers,” *IEEE Eng. Med. Biol. Mag.*, vol. 25, no. 3, pp. 38–48, 2006.
- [15] A. I. M. Deyell, S. Tung, “The implantable cardioverter-defibrillator: From Mirowski to its current use,” *B. C. Med. J.*, vol. 52, no. 5, pp. 248–253, 2010.
- [16] “By Bjorn Knetsch from The Netherlands (2009\_01\_20\_2352 Uploaded by tabercil) [CC BY 2.0 (<http://creativecommons.org/licenses/by/2.0>)], via Wikimedia Commons.” [Online]. Available: [http://commons.wikimedia.org/wiki/File/%3AInfant\\\_with\\\_cochlear\\\_implant.jpg](http://commons.wikimedia.org/wiki/File/%3AInfant\_with\_cochlear\_implant.jpg)
- [17] F.-G. Zeng, “Trends in Cochlear Implants,” *Trends Amplif.*, vol. 8, no. 1, pp. 1–34, 2004.
- [18] J. D. Weiland, W. Liu, and M. S. Humayun, “Retinal prosthesis,” *Annu. Rev. Rev. Biomed. Eng.*, vol. 7, pp. 361–401, 2005.
- [19] H. Fassbender, W. Mokwa, M. Gortz, K. Trieu, U. Urban, T. Schmitz-Rode, T. Gottsche, and P. Osypka, “Fully implantable blood pressure sensor for hypertonic patients,” in *Proc. IEEE Sensors*, Oct. 2008, pp. 1226–1229.
- [20] M. Ahmadi and G. Jullien, “A wireless-implantable microsystem for continuous blood glucose monitoring,” *IEEE Trans. Biomed. Circuits Syst.*, vol. 3, no. 3, pp. 169–180, 2009.
- [21] K. Wise, D. Anderson, J. Hetke, D. Kipke, and K. Najafi, “Wireless Implantable Microsystems: High-Density Electronic Interfaces to the Nervous System,” *Proc. of the IEEE*, vol. 92, no. 1, pp. 76–97, Jan. 2004.
- [22] A. L. Benabid, “Deep brain stimulation for Parkinson’s disease,” *Current Opin. Neurobiol.*, vol. 13, no. 6, pp. 696–706, Dec. 2003.
- [23] S. H. Kennedy, P. Giacobbe, S. J. Rizvi, F. M. Placenza, Y. Nishikawa, H. S. Mayberg, and A. M. Lozano, “Deep brain stimulation for treatment-resistant depression: follow-up after 3 to 6 years,” *Am. J. Psychiatry*, vol. 168, no. 5, pp. 502–510, May 2011.

- [24] G.-Z. E. Yang, *Body Sensor Networks*. Springer Science + Business Media B.V., 2006.
- [25] Y.-H. Joung, “Development of Implantable Medical Devices: From an Engineering Perspective,” *Int. Neurol. J.*, vol. 17, pp. 98–106, 2013.
- [26] Y. Zhang, F. Zhang, Y. Shakhsher, J. D. Silver, A. Klinefelter, M. Nagaraju, J. Boley, J. Pandey, A. Shrivastava, E. J. Carlson, A. Wood, B. H. Calhoun, and B. P. Otis, “A batteryless 19uW MICS/ISM-band energy harvesting body area sensor node SoC,” *IEEE J. Solid-State Circuits*, vol. 48, no. 1, pp. 199–213, 2013.
- [27] R. Vullers, R. van Schaijk, I. Doms, C. Van Hoof, and R. Mertens, “Micropower energy harvesting,” *Solid-State Electron.*, vol. 53, no. 7, pp. 684–693, Jul. 2009.
- [28] J. Olivo, S. Carrara, and G. De Micheli, “Energy Harvesting and Remote Powering for Implantable Biosensors,” *IEEE Sensors J.*, vol. 11, no. 7, pp. 1573–1586, Jul. 2011.
- [29] C. Lu, V. Raghunathan, and K. Roy, “Efficient Design of Micro-Scale Energy Harvesting Systems,” *IEEE J. Emerg. Sel. Topics Circuits Syst.*, vol. 1, no. 3, pp. 254–266, Sep. 2011.
- [30] J. Rabaey and F. Burghardt, “Energy harvesting-A systems perspective,” in *Proc. IEEE International Electron Devices Meeting*, 2007, pp. 363–366.
- [31] E. Torres and G. Rincón-Mora, “Energy-Harvesting System-in-Package Microsystem,” *J. Energ. Eng.-ASCE*, vol. 134, no. 4, pp. 121–129, 2008.
- [32] P. D. Mitcheson, “Energy harvesting for human wearable and implantable bio-sensors,” in *Proc. Annual International Conference of the Engineering in Medicine and Biology Society*, Jan. 2010, pp. 3432–6.
- [33] R. Vullers and R. Schaijk, “Energy harvesting for autonomous wireless sensor networks,” *IEEE Solid State Circuits Mag.*, vol. 2, no. 2, pp. 29–38, 2010.
- [34] A. Cadei, A. Dionisi, E. Sardini, and M. Serpelloni, “Kinetic and thermal energy harvesters for implantable medical devices and biomedical autonomous sensors,” *Meas. Sci. Technol.*, vol. 25, no. 1, pp. 1–14, 2014.
- [35] E. J. Carlson, K. Strunz, and B. P. Otis, “A 20 mV Input Boost Converter With Efficient Digital Control for Thermoelectric Energy Harvesting,” *IEEE J. Solid-State Circuits*, vol. 45, no. 4, pp. 741–750, Apr. 2010.
- [36] Y. K. Ramadass and A. P. Chandrakasan, “An Efficient Piezoelectric Energy Harvesting Interface Circuit Using a Bias-Flip Rectifier and Shared Inductor,” *IEEE J. Solid-State Circuits*, vol. 45, no. 1, pp. 189–204, Jan. 2010.

- [37] K. Kadirvel, Y. Ramadass, U. Lyles, J. Carpenter, V. Ivanov, V. McNeil, A. Chandrakasan, and B. Lum-Shue-Chan, "A 330nA energy-harvesting charger with battery management for solar and thermoelectric energy harvesting," in *IEEE Int. Solid-State Circuits Conf. Dig. Tech. Papers*, Feb. 2012, pp. 106–108.
- [38] S. Bandyopadhyay and A. P. Chandrakasan, "Platform architecture for solar, thermal and vibration energy combining with MPPT and single inductor," *IEEE J. Solid-State Circuits*, vol. 47, no. 9, pp. 2199–2215, 2011.
- [39] P.-H. Chen and P. M.-Y. Fan, "Multiple-Output Based Adaptive Gate Biasing DC-DC Converter for Thermoelectric Energy Harvesting," *IEEE Trans. Circuits Syst. I, Reg. Papers*, vol. 62, no. 2, pp. 405–412, 2015.
- [40] I. Doms, P. Merken, R. Mertens, and C. Van Hoof, "Integrated capacitive power-management circuit for thermal harvesters with output power 10 to 1000uW," in *IEEE Int. Solid-State Circuits Conf. Dig. Tech. Papers*, vol. 5, 2009, pp. 300–302.
- [41] X. Zhang, H. Ren, S. Pyo, J.-I. Lee, J. Kim, and J. Chae, "A High-Efficiency DC-DC Boost Converter for a Miniaturized Microbial Fuel Cell," *IEEE Trans. on Power Electron.*, vol. 30, no. 4, pp. 2041–2049, 2015.
- [42] B. H. Calhoun, S. Khanna, Y. Zhang, J. Ryan, and B. Otis, "System design principles combining sub-threshold circuit and architectures with energy scavenging mechanisms," *Proc. of IEEE International Symposium on Circuits and Systems*, pp. 269–272, May 2010.
- [43] M. Penella and M. Gasulla, "A review of commercial energy harvesters for autonomous sensors," *Proc. of Instrumentation and Measurement Technology Conference*, pp. 1–5, 2007.
- [44] A. P. Chandrakasan, D. C. Daly, J. Kwong, and Y. K. Ramadass, "Next generation micro-power systems," in *Proc. of IEEE Symposium on VLSI Circuits, Digest of Technical Papers*, 2008, pp. 2–5.
- [45] M. Pedram, N. Chang, Y. Kim, and Y. Wang, "Hybrid electrical energy storage systems," in *Proc. of ACM/IEEE International Symposium on Low-Power Electronics and Design*, 2010, pp. 363–368.
- [46] G. V. Merrett and A. S. Weddell, "Supercapacitor leakage in energy-harvesting sensor nodes: fact or fiction?" in *Proc. of International Conference on Networked Sensing Systems*, 2012, pp. 6–10.
- [47] A. Harb, "Energy harvesting: State-of-the-art," *Renew. Energ.*, vol. 36, no. 10, pp. 2641–2654, 2011.



- [48] G. Park, T. Rosing, M. D. Todd, C. R. Farrar, and W. Hodgkiss, "Energy Harvesting for Structural Health Monitoring Sensor Networks," *J. of Infrastruct. Syst.*, vol. 14, no. 1, pp. 64–79, 2008.
- [49] B. H. Calhoun, J. Lach, J. Stankovic, D. D. Wentzloff, K. Whitehouse, A. T. Barth, J. K. Brown, Q. Li, S. Oh, N. E. Roberts, and Y. Zhang, "Body sensor networks: A holistic approach from silicon to users," *Proc. of the IEEE*, vol. 100, no. 1, pp. 91–106, 2012.
- [50] D. L. Purdy, "Nuclear Batteries for Implantable Applications," in *Batteries for Implantable Biomedical Devices*, 1986, pp. 285–352.
- [51] C. Williams and R. Yates, "Analysis of a micro-electric generator for microsystems," in *Proc. of International Conference on Solid-State Sensors and Actuators*, 1995, pp. 369–372.
- [52] S. Roundy, P. K. Wright, and J. Rabaey, "A study of low level vibrations as a power source for wireless sensor nodes," *Comput. Commun.*, vol. 26, no. 11, pp. 1131–1144, Jul. 2003.
- [53] T. von Buren, P. D. Mitcheson, T. C. Green, E. M. Yeatman, A. S. Holmes, and G. Troster, "Optimization of inertial micropower generators for human walking motion," *IEEE Sensors J.*, vol. 6, no. 1, pp. 28–38, 2006.
- [54] R. Torah, S. Beeby, M. Tudor, T. O'Donnell, and S. Roy, "Development of a Cantilever Beam Generator Employing Vibration Energy Harvestin," *Proc. 6th int. workshop micro nanotech. power generation energy conversion app.*, no. 1, pp. 181–184, 2006.
- [55] H. Goto, T. Sugiura, Y. Harada, and T. Kazui, "Feasibility of using the automatic generating system for quartz watches as a leadless pacemaker power source," *Med. Biol. Eng. Comput.*, vol. 37, no. 3, pp. 377–80, May 1999.
- [56] G. Despesse and J. Chaillout, "Innovative structure for mechanical energy scavenging," in *Proc. of International Conference on Solid-State Sensors*, 2007, pp. 895–898.
- [57] P. Miao, P. D. Mitcheson, A. S. Holmes, E. M. Yeatman, T. C. Green, and B. H. Stark, "Mems inertial power generators for biomedical applications," *Microsyst. Technol.*, vol. 12, no. 1, pp. 1079–1083, Apr. 2006.
- [58] S. Roundy, E. Leland, J. Baker, E. Carleton, E. Reilly, E. Lai, B. Otis, J. Rabaey, V. Sundararajan, and P. Wright, "Improving Power Output for Vibration-Based Energy Scavengers," *IEEE Pervasive Comput.*, vol. 4, no. 1, pp. 28–36, Jan. 2005.

- [59] R. Elfrink, T. M. Kamel, M. Goedbloed, S. Matova, D. Hohlfeld, Y. van An-  
del, and R. van Schaijk, "Vibration energy harvesting with aluminum nitride-  
based piezoelectric devices," *J. Micromech. and Microeng.*, vol. 19, no. 9, pp.  
1–8, Sep. 2009.
- [60] M. Marzencki, Y. Ammar, and S. Basrour, "Integrated power harvesting sys-  
tem including a MEMS generator and a power management circuit," *Sens.*  
*Actuators A*, vol. 145–146, no. 1, pp. 363–370, Jul. 2008.
- [61] Perpetuum, "<http://www.perpetuum.com/>," 2010.
- [62] EnOcean, "<http://www.enocean.com/>," 2012.
- [63] M. D. Seeman, S. R. Sanders, and J. M. Rabaey, "An ultra-low-power power  
management IC for energy-scavenged Wireless Sensor Nodes," in *Proc. IEEE*  
*Power Electronics Specialists Conference*, Jun. 2008, pp. 925–931.
- [64] V. Leonov, T. Torfs, P. Fiorini, and C. Van Hoof, "Thermoelectric Converters  
of Human Warmth for Self-Powered Wireless Sensor Nodes," *IEEE Sensors*  
*J.*, vol. 7, no. 5, pp. 650–657, May 2007.
- [65] V. Leonov, "Thermal shunts in thermoelectric energy scavengers," *Journal of*  
*Electron. Mater.*, vol. 38, no. 7, pp. 1483–1490, 2009.
- [66] V. Leonov and P. Fiorini, "Thermal matching of a thermoelectric energy  
scavenger with the ambience," in *Proc. of the European Conference on Ther-*  
*moelectrics*, no. 3, 2007, pp. 129–133.
- [67] A. Chen and P. Wright, "Medical Applications of Thermoelectrics," in *Mod-*  
*ules, Systems, and Applications in Thermoelectrics*, 2012, pp. 1–22.
- [68] Y. Yang, X.-J. Wei, and J. Liu, "Suitability of a thermoelectric power gen-  
erator for implantable medical electronic devices," *J. Phys. D: Appl. Phys.*,  
vol. 40, no. 18, pp. 5790–5800, Sep. 2007.
- [69] Y. K. Ramadass and A. P. Chandrakasan, "A battery-less thermoelectric  
energy harvesting interface circuit with 35 mV startup voltage," *IEEE J.*  
*Solid-State Circuits*, vol. 46, no. 1, pp. 333–341, 2011.
- [70] Thermo Life, "<http://www.poweredbythermolife.com/>."
- [71] Nextreme, "<http://www.nextreme.com/>."
- [72] Tellurex, "<http://www.tellurex.com/>."
- [73] Micropelt, "<http://www.micropelt.com/>," 2014.
- [74] H. Sakai, "Sony Develops "Bio Battery" that Generates Electricity from  
Sugar," Sony Corporation, Tech. Rep., 2007.

- [75] F. Davis and S. P. J. Higson, "Biofuel cells—recent advances and applications." *Biosens. Bioelectron.*, vol. 22, no. 7, pp. 1224–1235, Feb. 2007.
- [76] A. Heller, "Miniature biofuel cells," *Phys. Chem. Chem. Phys.*, vol. 6, no. 2, pp. 209–216, 2004.
- [77] P. Cinquin, C. Gondran, F. Giroud, S. Mazabrard, A. Pellissier, F. Boucher, J.-P. Alcaraz, K. Gorgy, F. Lenouvel, S. Mathé, P. Porcu, and S. Cosnier, "A glucose biofuel cell implanted in rats." *PloS one*, vol. 5, no. 5, pp. 1–7, Jan. 2010.
- [78] J. Niessen, U. Schroder, and F. Scholz, "Exploiting complex carbohydrates for microbial electricity generation - a bacterial fuel cell operating on starch," *Electrochem. Commun.*, vol. 6, no. 9, pp. 955–958, Sep. 2004.
- [79] S. Kerzenmacher, J. Ducrée, R. Zengerle, and F. von Stetten, "An abiotically catalyzed glucose fuel cell for powering medical implants: Reconstructed manufacturing protocol and analysis of performance," *J. of Power Sources*, vol. 182, no. 1, pp. 66–75, Jul. 2008.
- [80] B. I. Rapoport, J. T. Kedzierski, and R. Sarpeshkar, "A glucose fuel cell for implantable brain-machine interfaces." *PloS ONE*, vol. 7, no. 6, pp. 1–15, Jan. 2012.
- [81] B. Cook, S. Lanzisera, and K. Pister, "SoC Issues for RF Smart Dust," *Proc. of the IEEE*, vol. 94, no. 6, pp. 1177–1196, Jun. 2006.
- [82] S. Kim, R. Vyas, J. Bito, K. Niotaki, A. Collado, A. Georgiadis, and M. M. Tentzeris, "Ambient RF Energy-Harvesting Technologies for Self-Sustainable Standalone Wireless Sensor Platforms," *Proc. of the IEEE*, vol. 102, no. 11, pp. 1649–1666, 2014.
- [83] Y.-S. Hwang, C.-C. Lei, Y.-W. Yang, J.-J. Chen, and C.-C. Yu, "A 13.56-MHz low-input and low-control-loss RF-DC rectifier utilizing a reducing reverse loss technique," *IEEE J. Solid-State Circuits*, vol. 29, no. 12, pp. 6544–6554, 2014.
- [84] C. Xu, C. Pan, Y. Liu, and Z. L. Wang, "Hybrid cells for simultaneously harvesting multi-type energies for self-powered micro/nanosystems," *Nano Energy*, vol. 1, no. 2, pp. 259–272, 2012.
- [85] C. Pan, Z. Li, W. Guo, J. Zhu, and Z. L. Wang, "Fiber-based hybrid nanogenerators for/as self-powered systems in biological liquid," *Angew. Chem. Int. Ed.*, vol. 50, pp. 11 192–11 196, 2011.
- [86] G. Villar-Piqué, H. Bergveld, and E. Alarcón, "Survey and benchmark of Fully Integrated Switching Power Converters: Switched-Capacitor vs Inductive approach," *IEEE Trans. Power Electron.*, vol. 28, no. 9, pp. 4156–4167, 2013.

- [87] T. Breussegeem and M. Steyaert, "A 82% efficiency 0.5% ripple 16-phase fully integrated capacitive voltage doubler," in *Proc. of Symposium on VLSI Circuits Digest Papers*, 2009, pp. 198–199.
- [88] C. Lu, S. P. Park, V. Raghunathan, and K. Roy, "Efficient power conversion for ultra low voltage micro scale energy transducers," in *Proc. of Design, Automation & Test in Europe Conference & Exhibition*, Mar. 2010, pp. 1602–1607.
- [89] S. Abdelaziz, A. Emira, A. G. Radwan, A. N. Mohieldin, and A. M. Soliman, "A low start up voltage charge pump for thermoelectric energy scavenging," in *Proc. of IEEE International Symposium on Industrial Electronics*. Ieee, Jun. 2011, pp. 71–75.
- [90] J. Kim, P. K. T. Mok, and C. Kim, "A 0.15 V Input Energy Harvesting Charge Pump With Dynamic Body Biasing and Adaptive Dead-Time for Efficiency Improvement," *IEEE J. Solid-State Circuits*, vol. 50, no. 2, pp. 414–425, 2015.
- [91] H. Le, S. Sanders, and E. Alon, "Design techniques for fully integrated switched-capacitor DC-DC converters," *IEEE J. Solid-State Circuits*, vol. 46, no. 9, pp. 2120–2131, 2011.
- [92] R. Grezaud and J. Willemin, "A self-starting fully integrated auto-adaptive converter for battery-less thermal energy harvesting," in *IEEE International New Circuits and Systems Conference, NEWCAS 2013*, 2013.
- [93] M. Makowski and D. Maksimovic, "Performance limits of switched-capacitor DC-DC converters," in *Proc. of IEEE Power Electronics Specialists Conference*, 1995, pp. 1215–1221.
- [94] H. Lhermet, C. Condemine, M. Plissonnier, R. Salot, P. Audebert, and M. Rosset, "Efficient Power Management Circuit: From Thermal Energy Harvesting to Above-IC Microbattery Energy Storage," *IEEE J. Solid-State Circuits*, vol. 43, no. 1, pp. 246–255, Jan. 2008.
- [95] P.-S. Weng, H.-Y. Tang, P.-C. Ku, and L.-H. Lu, "50 mV-Input Battery-less Boost Converter for Thermal Energy Harvesting," *IEEE J. Solid-State Circuits*, vol. 48, no. 4, pp. 1031–1041, Apr. 2013.
- [96] J.-P. Im, S.-W. Wang, S.-T. Ryu, and G.-H. Cho, "A 40 mV Transformer-Reuse Self-Startup Boost Converter With MPPT Control for Thermoelectric Energy Harvesting," *IEEE J. Solid-State Circuits*, vol. 47, no. 12, pp. 3055–3067, Dec. 2012.
- [97] S. Bandyopadhyay, P. P. Mercier, A. C. Lysaght, K. M. Stankovic, and A. P. Chandrakasan, "A 1.1 nW Energy-Harvesting System with 544 pW Quiescent Power for Next-Generation Implants," *IEEE J. Solid-State Circuits*, vol. 49, no. 12, pp. 1–13, 2014.

- [98] M. Wens, K. Cornelissens, and M. Steyaert, "A fully-integrated 0.18 $\mu$ m CMOS DC-DC step-up converter, using a bondwire spiral inductor," *Proc. of the European Solid-State Circuits Conference*, pp. 268–271, 2007.
- [99] R. W. Erickson and D. Maksimovic, *Fundamentals of Power Electronics*, 2nd ed. Springer Science + Business Media B.V., 2002.
- [100] A. J. Stratakos, S. R. Sanders, and R. W. Brodersen, "A low-voltage CMOS DC-DC converter for a portable battery-operated system," in *Proc. of Power Electronics Specialist Conference*, 1994.
- [101] Z. Sun, K. W. R. Chew, H. Tang, and L. Siek, "Adaptive gate switching control for discontinuous conduction mode DC-DC converter," *IEEE Trans. on Power Electron.*, vol. 29, no. 3, pp. 1311–1320, 2014.
- [102] J. Katic, S. Rodriguez, and A. Rusu, "Analysis of Dead Time Losses in Energy Harvesting Boost Converters for Implantable Biosensors," in *Proc. IEEE International conference NORCHIP*, 2014, pp. 1–4.
- [103] P.-H. Chen, K. Ishida, K. Ikeuchi, X. Zhang, K. Honda, Y. Okuma, Y. Ryu, M. Takamiya, and T. Sakurai, "Startup Techniques for 95 mV Step-Up Converter by Capacitor Pass-On Scheme and Vth-Tuned Oscillator With Fixed Charge Programming," *IEEE J. Solid-State Circuits*, vol. 47, no. 5, pp. 1252–1260, 2012.
- [104] P. P. Mercier, S. Bandyopadhyay, A. C. Lysaght, K. M. Stankovic, and A. P. Chandrakasan, "A Sub-nW 2.4 GHz transmitter for low data-rate sensing applications," *IEEE J. of Solid-State Circuits*, vol. 49, no. 7, pp. 1463–1474, 2014.
- [105] J. Katic, S. Rodriguez, and A. Rusu, "An Efficient Boost Converter Control for Thermoelectric Energy Harvesting," in *Proc. IEEE International Conference on Electronics, Circuits and Systems (ICECS)*, 2013, pp. 385–388.
- [106] A. P. Chandrakasan and R. W. Brodersen, "Minimizing power consumption in digital CMOS circuits," *Proc. of the IEEE*, vol. 83, no. 4, pp. 498–523, 1995.
- [107] T. Y. Man, P. K. T. Mok, and M. J. Chan, "A 0.9-V input discontinuous-conduction-mode boost converter with CMOS-control rectifier," *IEEE J. Solid-State Circuits*, vol. 43, no. 9, pp. 2036–2046, 2008.
- [108] M. Wens and M. Steyaert, *Design and Implementation of Fully-Integrated Inductive DC-DC Converters in Standard CMOS*. Springer, 2011.
- [109] K. Ueno, T. Hirose, T. Asai, and Y. Amemiya, "A 300 nW, 15 ppm/ $^{\circ}$ C, 20 ppm/V CMOS voltage reference circuit consisting of subthreshold MOS-FETs," *IEEE J. Solid-State Circuits*, vol. 44, no. 7, pp. 2047–2054, 2009.

- [110] X. Zhang and A. B. Apsel, “A Low-Power, Process-and- Temperature- Compensated Ring Oscillator With Addition-Based Current Source,” *IEEE Trans. Circuits Syst. I, Reg. Papers*, vol. 58, no. 5, pp. 868–878, 2011.
- [111] D. Markovic, B. Nikolic, and W. B. Brodersen, “Analysis and Design of Low-Energy Flip-Flops,” in *Proc. of International Symposium on Low Power Electronics and Design*, 2001, pp. 52–55.